

POLITECNICO DI TORINO

Department of Environment, Land and Infrastructure Engineering



Master of Science in Petroleum and
Mining Engineering

Surface Wave Tomography applied to Oil and Gas Data

Supervisor:
Prof. Laura Valentina Socco
Co-supervisor:
Farbod Khosro Anjom

Student:
Michel Tawil

Academic year 2018-2019

December, 2019

ACKNOWLEDGEMENTS

I would like to thank my supervisor, Professor Laura Valentina Socco, for the patient guidance, encouragement and continual support she has provided throughout the whole period of the project. I have been extremely lucky to have a supervisor who has been very helpful, cared so much about my work and responded to all my questions and doubts related to the project.

A special thanks to my co-supervisor Farbod Khosro Anjom for his contribution to the work, he has been extremely helpful, answering all my questions so promptly, clarifying all my doubts and helping me find solutions to all the problems I encountered. I would also like to express my gratitude for the team working with Professor Socco: Myrto, Federico and Karimpour.

I would also like to thank TOTAL E&P for providing the real data and giving us the show right.

I would like to thank all my professors at the Lebanese University-Faculty of Engineering, specially to Dr. Azzi, Dr. Hobeika, and to my supervisor Dr. Marlene Cordahi who did not participate directly in the development of this thesis but was very helpful and supportive not only in this period but also during my Bachelor's degree.

Completing this work would have been all the more difficult were it not for the support of my family. I really thank you for being by my side in every decision I made. A special thanks to Ana and Nicole who were listening and supporting me when I needed them the most.

Finally, I would like to thank Politecnico di Torino and the Italian Ministry of External Affairs for the scholarships they granted me during my exchange program.

November 2019,

Michel Tawil.

ABSTRACT

For land acquisition, the existence of shallow low-velocity heterogeneous layers makes the imaging of the deep seismic reflection inconsistent. This issue is, commonly, addressed by performing static corrections on the data. An effective static correction requires a reliable model of the near-surface. Surface wave (SW) tomography is a powerful tool to estimate the shallow subsurface. Given good data coverage, SW tomography is expected to provide a reliable and high-resolution estimation of near-surface shear wave velocity (VS). We present the application of SW tomography to a 2D dataset acquired for hydrocarbon exploration purposes. The processing to extract the dispersion curves (DCs) is performed using a two-station method that consists of computing the average phase slowness for each receiver pair illuminated by a source. The DCs extracted are then inverted using damped least square method, to obtain a VS model representative of the shallow subsurface. Finally, the inversion is validated using a checkerboard test. A novel representation of coverage for 2D data is developed (in MATLAB).

Keywords: Surface wave tomography; Inversion; Shallow subsurface; Shear wave velocity (VS).

TABLE OF CONTENTS

LIST OF FIGURES	vii
LIST OF TABLES	xii
LIST OF ACRONYMS AND SYMBOLS	xiii
Chapter 1 : Introduction	1
Chapter 2 : Method	4
2.1 Seismic waves	4
2.1.1 Body waves	4
2.1.1.1 Compressional wave.....	4
2.1.1.2 Shear wave	4
2.1.2 Surface waves	5
2.1.2.1 Love wave.....	5
2.1.2.2 Rayleigh wave.....	6
2.2 Geometrical dispersion	8
2.3 Surface Wave Tomography	10
2.3.1 Data acquisition	12
2.3.2 Processing.....	12
2.3.2.1 Group velocities and time windowing.....	13
2.3.2.2 Cross-correlation and phase velocity computation.....	14

2.3.3 Inversion	15
2.3.3.1 Forward Problem	15
2.3.3.2 Inversion Algorithm	16
2.4 Checkerboard Test.....	18
Chapter 3 : Data, Processing and Results	20
3.1 Data	20
3.1.1 Test site	20
3.2 Processing.....	22
3.2.1 Processing example	23
3.3 Results	25
3.3.1 Dispersion Curves	25
3.3.2 Coverage	27
3.3.3 Inversion	30
3.3.3.1 Inversion 1: unconstrained.....	32
3.3.3.2 Inversion 2: lateral constraint equal to 400 m/s.....	34
3.3.3.3 Inversion 3: lateral constraint equal to 200 m/s.....	36
3.3.3.4 Inversion 4: lateral constraint equal to 100 m/s.....	38
3.3.3.5 Inversion 5: broken lateral constraint equal to 100 m/s.	42
3.3.4 Checkerboard test	48

Chapter 4 : Discussion and Conclusion	53
REFERENCES	55
APPENDIX A	59
Example 1: Short offset	60
Example 2: Long offset.....	61
Example 3: Optimal offset range.....	62
Example 4: Minimum inter-receivers distance	65
Example 5: Maximum inter-receivers distance.....	68

LIST OF FIGURES

Figure 2.1: Direction of propagation and evolution of body waves with time T: a) P-wave b) S-wave. X and Y are parallel to the surface while Z is the depth. Particles are represented by cubes in these two models (Braile 2006).	5
Figure 2.2: Direction of propagation and evolution of surface waves with time T: a) Love wave b) Rayleigh wave. X and Y are parallel to the surface while Z is the depth. Particles are represented by cubes in these two models (Braile 2006).....	7
Figure 2.3: Normalized vertical and radial displacements of Rayleigh waves with respect to the wavelength as a function of: a) the individual displacements vertical and radial components, b) the elliptical motion changing with depth from retrograde ellipse to linear vertical then to prograde ellipse. Modified from Gedge and Hill, 2012.	8
Figure 2.4: Schematic representation of geometric dispersion of Rayleigh waves: the vertical displacement associated with a short and a long wavelength (Socco and Strobbia, 2004). λ_1 covers a homogeneous medium while λ_2 covers a vertically heterogeneous subsurface. The arrow represents the shot.	9
Figure 2.5: An example of modal curves (Socco and Strobbia, 2004)	10
Figure 2.6: Workflow diagram of the process applied to extract the DCs.....	13
Figure 2.7: The solid line represents the path of the circle propagation between two stations A and B. The phase slowness p_i at any point i along a path is determined from the values at four surrounding points.	16
Figure 2.8: Scheme of positive and negative 15 percent perturbation.	19
Figure 3.1: A scheme of the location where the dataset was acquired along a seismic line (modified from Masoni, 2016). The black double arrow shows the portion of the line in which the data were processed in the present work.	21

Figure 3.2: Scheme showing the configuration of sources and receivers along the analyzed 4 km (∇ - receivers, * - shots).	21
Figure 3.3: Computed spectrum of the first receiver: a) picked group velocity vs frequency and b) time vs frequency.	24
Figure 3.4: Computed spectrum of the second receiver: a) picked group velocity vs frequency and b) time vs frequency.	24
Figure 3.5: DC for shot number 50 and receiver pair 9&16: a) The cross multiplication matrix of the two traces b) Picked DC.....	25
Figure 3.6: DCs plotted as phase velocity vs frequency.	26
Figure 3.7: DCs plotted as wavelength vs phase velocity.	27
Figure 3.8: The coverage (number of paths) at the position of each model point shown at each frequency.	28
Figure 3.9: The coverage (number of paths) at the position of each model point shown at each wavelength.	29
Figure 3.10: Representation of each path with a color that corresponds to the average phase velocity at the given wavelength.....	30
Figure 3.11: A homogeneous Initial model composed of 30 1D models and 12 layers above half space. The velocity of all layers is 1100 m/s.	32
Figure 3.12: Inverted model for unconstrained inversion.	33
Figure 3.13: Misfit corresponding to the 1st inversion. 28 iterations needed to reach the lowest misfit.	33
Figure 3.14: Misfit of the DCs of different paths for inversion 1.....	34
Figure 3.15: Inverted model for Inversion 2 (inversion parameters in table 3.2).	35

Figure 3.16: Misfit corresponding to the 2nd inversion. 28 iterations needed to reach the lowest misfit.	35
Figure 3.17: Misfit of the DCs of different paths for inversion 2.....	36
Figure 3.18: Inverted model for Inversion 3 (inversion parameters in table 3.2)	37
Figure 3.19: Misfit corresponding to the 3 rd inversion. 26 iterations needed to reach the lowest misfit.	37
Figure 3.20: Misfit of the DCs of different paths for inversion 3.....	38
Figure 3.21: Inverted model for Inversion 4 (inversion parameters in table 3.2).	39
Figure 3.22: Misfit corresponding to the 4th inversion. 28 iterations needed to reach the lowest misfit.	40
Figure 3.23: Misfit of the DCs of different paths for inversion 4.....	41
Figure 3.24: Comparison between 2D VS models obtained by a) surface wave tomography, b) surface wave direct transform (Khosro Anjom et al., 2019) and c) SWODI (Masoni, 2016).	42
Figure 3.25: Misfit corresponding to the 5 th inversion. 26 iterations needed to reach the lowest misfit.	43
Figure 3.26: Misfit of the DCs of different paths for inversion 5.....	44
Figure 3.27: Fitting of experimental and theoretical DCs for path number 51 for different inversions.....	45
Figure 3.28: Fitting of experimental and theoretical DCs for path number 193 for different inversions.....	46
Figure 3.29: Fitting of experimental and theoretical DCs for path number 209 for different inversions.....	47

Figure 3.30: Fitting of experimental and theoretical DCs for path number 220 for different inversions.....	48
Figure 3.31: Checkerboard initial VS model.....	49
Figure 3.32: Scheme of positive and negative 15 percent perturbation.	50
Figure 3.33: Perturbed model obtained by the multiplication of the initial model by the perturbation.....	50
Figure 3.34: Inverted model obtained by the checkerboard test.	51
Figure 3.35: Misfit corresponding to the checkerboard test. 28 iterations needed to reach the lowest misfit.	52
Figure A.1: DC for shot number 68 and receiver pair 20&22: a) The windowed cross multiplication matrix of the two traces b) Picked DC.	61
Figure A.2: DC for shot number 43 and receiver pair 20&22: a) The windowed cross multiplication matrix of the two traces b) Picked DC.	62
Figure A.3: DC for shot number 66 and receiver pair 20&22: a) The windowed cross multiplication matrix of the two traces b) Picked DC.	63
Figure A.4: DC for shot number 61 and receiver pair 20&22: a) The windowed cross multiplication matrix of the two traces b) Picked DC.	64
Figure A.5: DC for shot number 53 and receiver pair 20&22: a) The windowed cross multiplication matrix of the two traces b) Picked DC.	65
Figure A.6: DC for shot number 42 and receiver pair 1&2: a) The windowed cross multiplication matrix of the two traces b) Picked DC.	66
Figure A.7: DC for shot number 42 and receiver pair 1&3: a) The windowed cross multiplication matrix of the two traces b) Picked DC.	67

Figure A.8: DC for shot number 42 and receiver pair 1&4: a) The windowed cross multiplication matrix of the two traces b) Picked DC.	68
Figure A.9: DC for shot number 42 and receiver pair 1&8: a) The windowed cross multiplication matrix of the two traces b) Picked DC.	69
Figure A.10: DC for shot number 42 and receiver pair 1&9: a) The windowed cross multiplication matrix of the two traces b) Picked DC.	70

LIST OF TABLES

Table 3.1: Receiver pairs used for each shot.....	23
Table 3.2: The settings for each inversion.	31
Table 3.3: The settings for the checkerboard test.	49
Table A.1: Source and receivers' configuration for each example.	60

LIST OF ACRONYMS AND SYMBOLS

DC	Dispersion curve
e	Variance
f	Frequency
G	Jacobian matrix
H	Horizontal constraint
LCI	Laterally constrained inversion
MASW	Multi-channel analysis of surface waves
P-wave	Primary wave/Compressional wave
RMS	Root mean square
S-wave	Secondary wave/Shear wave
SW	Surface wave
SWODI	Surface wave 1D inversion
S/N	Signal to noise ratio
T	Time
V	Phase velocity
VP	Primary wave velocity
VS	Shear wave velocity
1D	One-dimensional
2D	Two-dimensional
3D	Three-dimensional
λ	wavelength
∇	Receivers
*	Shots

Chapter 1: Introduction

Seismic exploration is the process of searching for economic deposits of crude oil, natural gas, and minerals using seismic techniques. Active seismic methods consist of recording, processing, and interpretation of artificially induced shock waves in the earth.

In oil and gas exploration, although the goal is the deep imaging of the subsurface, the reconstruction of the near-surface velocity models is an essential step. The seismic signals recorded at the surface are recorded in the time domain. The propagation of the seismic wavefield through the low-velocity heterogeneous layers (weathering layers), at the shallow subsurface, onshore, can significantly affect the consistency of deep reflectors in the final seismic image by masking the reflection data. Hence, the data are commonly corrected (static corrections) to remove the effect of the weathering layers (Berni and Roever, 1989) using the near-surface estimation of the velocity models.

Several approaches can be used to estimate the near-surface velocity models such as seismic reflection and refraction, (Burger et al., 1992). However, the data processing of the shallow subsurface encounters challenges when using seismic reflection such as attenuation of high frequency and aliasing (Steeple, 2000; Al-Anezi et al., 2011). Recently, the interest in surface waves has been increased to characterize the near-surface because they carry plenty of information.

Surface waves propagate close to the surface and parallel to the free surface and they are usually the dominant waves in the recordings. Surface waves are, usually, considered noise in seismic reflection methods (Dobrin, 1950), and they are filtered out from the recordings.

Surface wave methods (SWMs) applied to the ground roll present in exploration seismic records can be used to retrieve S-wave velocity models. Multichannel analysis of surface waves (MASW) is the most popular method to estimate the dispersion curves (DCs) (phase velocity vs frequency/wavelength) for near-surface wave velocity

characterization because of its ability to distinguish the fundamental modes of surface waves from the body waves or higher modes. However, it is difficult to estimate the strong lateral variations accurately by MASW-based approach (Ikeda and Tsuji, 2018). On the other hand, given a good data coverage, surface wave tomography can provide a high-resolution VS model of the subsurface and recover lateral variations (Shapiro et al., 2005; Yao et al., 2006). It has an advantage of a good compromise between horizontal and vertical resolutions compared to other methods (Salaün et al., 2012). Surface wave tomography consists of extracting the (DCs) using a two-station method and inverting the corresponding DCs in a tomographic way to obtain the S-wave model.

In the two-station method, an adequate time windowing should be used to overcome the limitations regarding the noise and isolation of higher modes (Yao et al., 2005). It is important to adopt an optimal offset between the source and two receivers as well as the inter-receiver distance: short and long offsets could narrow the frequency band of the DCs obtained. In addition, a high number of overlapping paths must be used to increase the data coverage and reliability of the inversion. The retrieved DCs are inverted by a tomographic inversion method developed in MATLAB by Boiero (2009). It is performed using an efficient weighted least square method and inverts directly for VS models (Papadopoulou et al., 2019). The experimental data are compared with the simulated data generated model until the lowest possible misfit is reached. The influence of parametrization and data coverage on the inversion performed is tested using a checkerboard test.

We implemented a novel method, in MATLAB, to present the data coverage by plotting the paths between each receiver pairs according to their average phase velocity within the wavelength range. The aim of this method is to detect the lateral and horizontal variations along the seismic line vs depth before inverting. This could help with choosing the lateral constraints for inversions. The assessment is carried out using Oil and Gas large scale exploration dataset provided by Total E&P to invert for the near-surface VS. Many studies have been carried on the same data: Masoni (2016), Karimpour (2018) and Khosro Anjom et al. (2019) for different purposes. The results of these studies are compared with the results of the surface wave tomography.

In this study, firstly, in chapter 2, the theoretical background related to seismic waves is presented. The body and surface waves are addressed, their types and main features of their propagation. Then, the most widely surface wave used, Rayleigh wave, as well as its dispersion characteristics, is described in more detail. Then, the surface wave tomography method is explained and a brief review of its application on local, regional and global scales to estimate the 2D VS models is provided. Followed by a brief explanation of optimal acquisition settings for surface wave tomography, the two main stages of surface wave tomography workflow is explained: processing and inversion. The processing consists of picking group velocities corresponding to the source and receiver pairs, applying a time window, cross-correlating the windowed traces and picking the cross-correlated maxima to extract the DCs. Then, the inversion algorithm implemented by Boiero (2009), is presented in detail in order to invert for VS model. An Appendix is attached to this study, showing the different tests carried on the data to obtain an optimal offset range as well as the optimal inter-receivers distance that are used for the processing for this specific dataset.

In chapter 3, the real data are presented, processed and inverted. The processing part provides the different configuration of shots and receivers performed to extract the DCs and an example of the processing. In the results part, the DCs extracted as well as the obtained data coverage, are shown. Five inversions were performed considering different lateral constraints. The purpose behind using different lateral constraint is to limit the solution non-uniqueness (Socco et al., 2009) by preventing the updates in neighboring models by more than the amount of the specified constraint. This leads to a smoother results if the misfit is kept low. The results of this study are compared to the other two studies carried on the same data (Masoni 2016; Khosro Anjom et al., 2019). A checkerboard of a specific perturbation percentage and block sizes is performed to validate the tomographic inversion.

Finally, In the last chapter, the results and the method are discussed.

Chapter 2: Method

We will begin by introducing seismic waves and specifically surface waves, their types, properties and their propagation characteristics. Then, we fully introduce the surface wave tomography method which we later use to estimate the VS model.

2.1 Seismic waves

Seismic waves are a periodic vibrational disturbance in which the energy is propagated through or along the surface of a medium. Based on their properties and propagation characteristics, they are classified into two categories: waves propagating in all directions from the source and hence travel through the earth's interior, called body waves, and waves travelling along the free surface, called surface waves (Evans and Dragoset, 1997).

2.1.1 Body waves

2.1.1.1 Compressional wave

Compressional waves (P-waves) are elastic waves in which particles oscillate in the direction of the propagation. P-wave is the fastest seismic wave and, consequently, the first to be recorded at a seismic station. It propagates through solid and fluid layers inside the earth. The direction of propagation of P-wave, as well as its evolution with time are shown in figure 2.1.

2.1.1.2 Shear wave

Shear waves (S-waves) are elastic waves in which particles oscillate perpendicular to the direction in which the wave propagates as shown in figure 2.1. They travel more slowly than P-waves, and as shear stress is nonexistent in fluids, they only travel through solids.

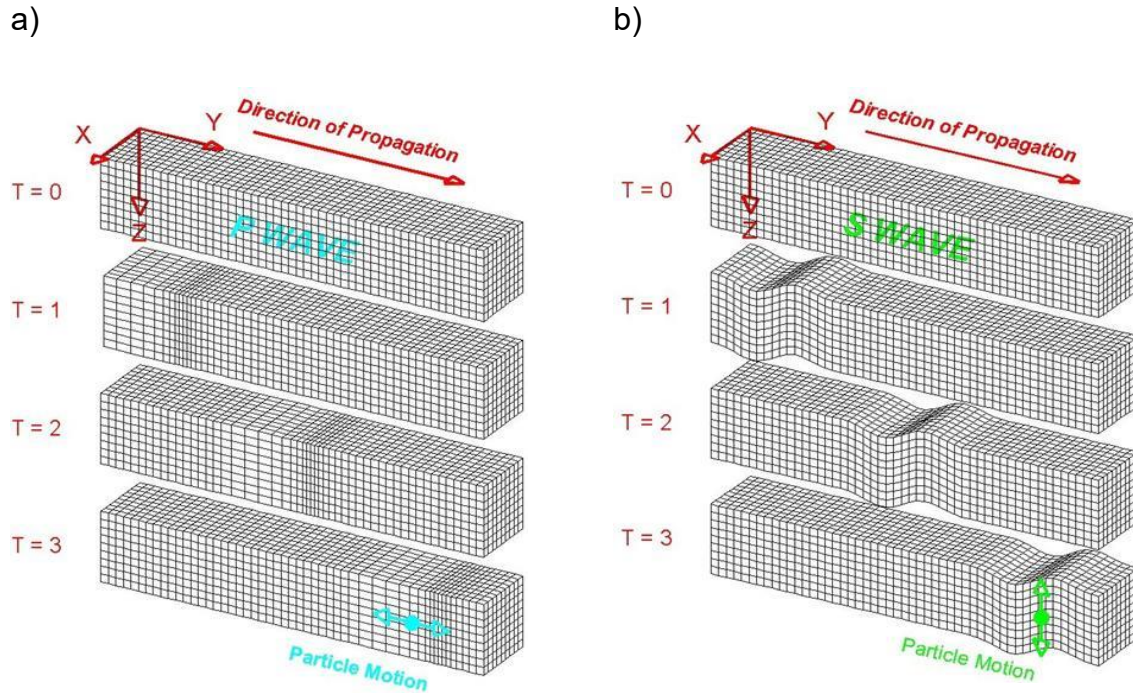


Figure 2.1: Direction of propagation and evolution of body waves with time T : a) P-wave b) S-wave. X and Y are parallel to the surface while Z is the depth. Particles are represented by cubes in these two models (Braile 2006).

2.1.2 Surface waves

Surface waves propagate parallel to the surface. There are several types of surface waves such as Lamb, Love, Scholte, Rayleigh, etc. The most widely used waves are Love waves and Rayleigh waves. In this thesis, Rayleigh waves are used to extract DCs that are used to perform a tomographic inversion.

2.1.2.1 Love wave

Love wave is named after A.E.H. Love, a British mathematician who worked out the mathematical model for this kind of wave (Love, 1911). It is the fastest type of surface waves in which particles oscillate horizontally and perpendicularly to the direction of wave propagation as shown in figure 2.2 (Braile, 2006).

2.1.2.2 Rayleigh wave

Rayleigh wave is named after Lord Rayleigh, who mathematically predicted the existence of this kind of wave (Strutt, 1885). Rayleigh waves create elliptical particle motion (figure 2.2). Figure 2.3 shows in a), the vertical and radial displacements of Rayleigh waves normalized to the wavelength as a function of the individual displacement components and in b) the particle motion in Rayleigh wave with depth in a homogeneous half space. At the top of the elliptical path, particle motion is anti-clockwise, and at the bottom it is clockwise. In between, it is vertical.

Usually, Rayleigh waves are the dominant waves in the seismic recordings (Woods, 1968). The energy decreases rapidly with depth and the particle displacements become negligible at a depth roughly equal to a wavelength (Athanapoulus et al., 2000). The wavefront is hence cylindrical and this affects the attenuation due to geometrical spreading. The energy density over the wavefront varies horizontally as $\frac{E}{2\pi r}$ where E is the energy and r is the distance travelled, their amplitude decreases proportionally to $\frac{1}{\sqrt{r}}$ (unlike body waves intensity that varies as $\frac{E}{\pi r^2}$ and their amplitude decreases as $\frac{1}{r}$ due to spherical spreading), they are the most energetic at distant offset.

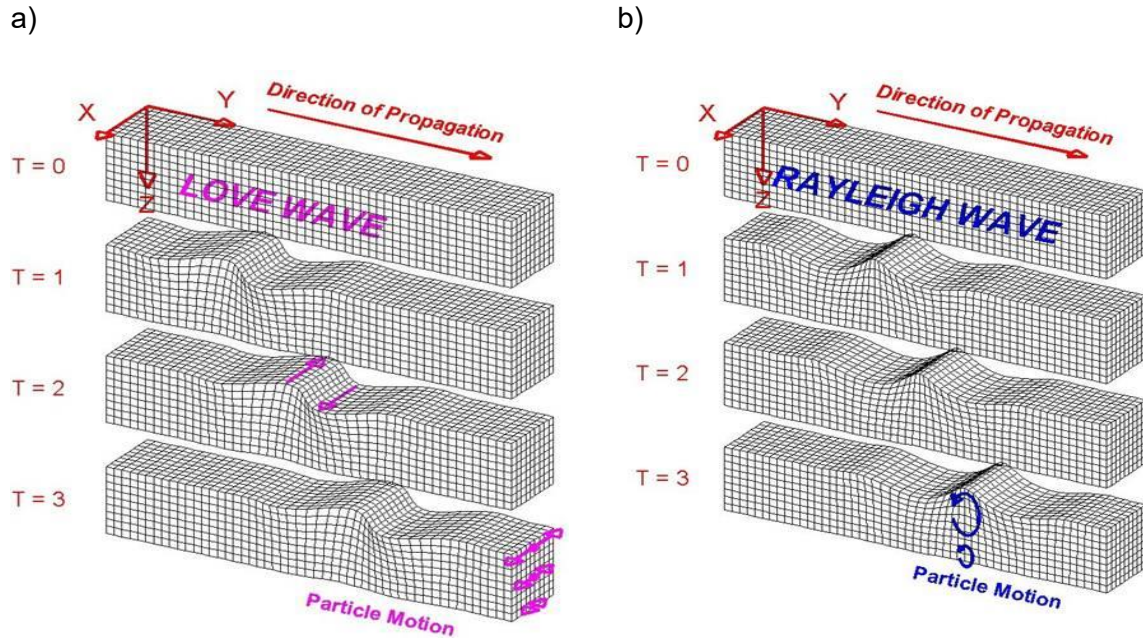


Figure 2.2: Direction of propagation and evolution of surface waves with time T : a) Love wave b) Rayleigh wave. X and Y are parallel to the surface while Z is the depth. Particles are represented by cubes in these two models (Braile 2006).

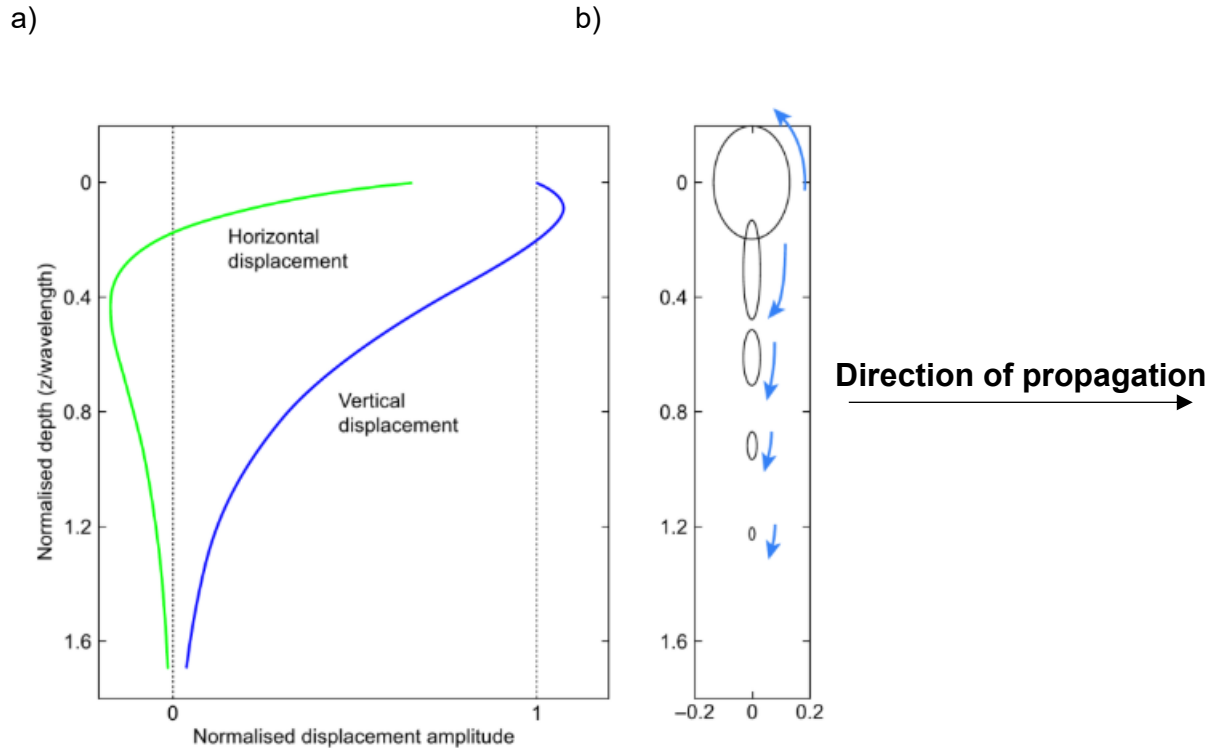


Figure 2.3: Normalized vertical and radial displacements of Rayleigh waves with respect to the wavelength as a function of: a) the individual displacements vertical and radial components, b) the elliptical motion changing with depth from retrograde ellipse to linear vertical then to prograde ellipse. Modified from Gedge and Hill, 2012.

2.2 Geometrical dispersion

In vertically heterogeneous media (layered systems), the different frequency components of the wavefield travel with different wavelengths depending on the velocity of propagation through the subsurface. High frequencies, short wavelengths, propagate close to the surface while low frequencies, long wavelengths, penetrate deeper portions of the subsurface and are affected also by the properties of deeper layers as shown in figure 2.4. As a result, the velocity of the surface wave is wavelength (frequency) dependent which is related to the geometrical distribution of the seismic velocity with depth. This kind of dispersion is hence called geometrical dispersion.

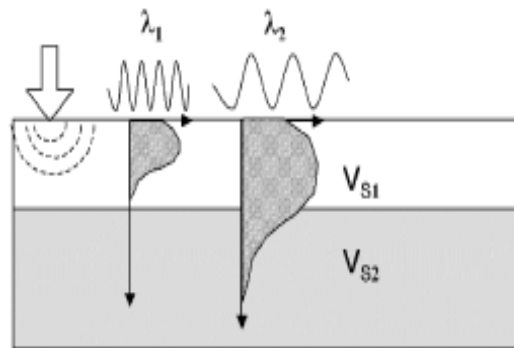


Figure 2.4: Schematic representation of geometric dispersion of Rayleigh waves: the vertical displacement associated with a short and a long wavelength (Socco and Strobba, 2004). λ_1 covers a homogeneous medium while λ_2 covers a vertically heterogeneous subsurface. The arrow represents the shot.

The DC is a representation of the phase velocity as a function of frequency or wavelength that depends on the vertical distribution of seismic velocities (P-wave velocity (V_P) and V_S) as well as the density of the medium. In most surface wave methods, the DCs are used to reconstruct the near-surface velocity model.

In layered media, the Rayleigh wave propagation is a modal phenomenon: at a given frequency there are several possible phase velocities that correspond to different vibration modes. Except for the first mode, called fundamental mode, each mode has limited frequency band and exists above a cut-off frequency. An example of modal curves is shown in figure 2.5. The surface wave used is Rayleigh wave and it will be referred as surface wave in the following chapters.

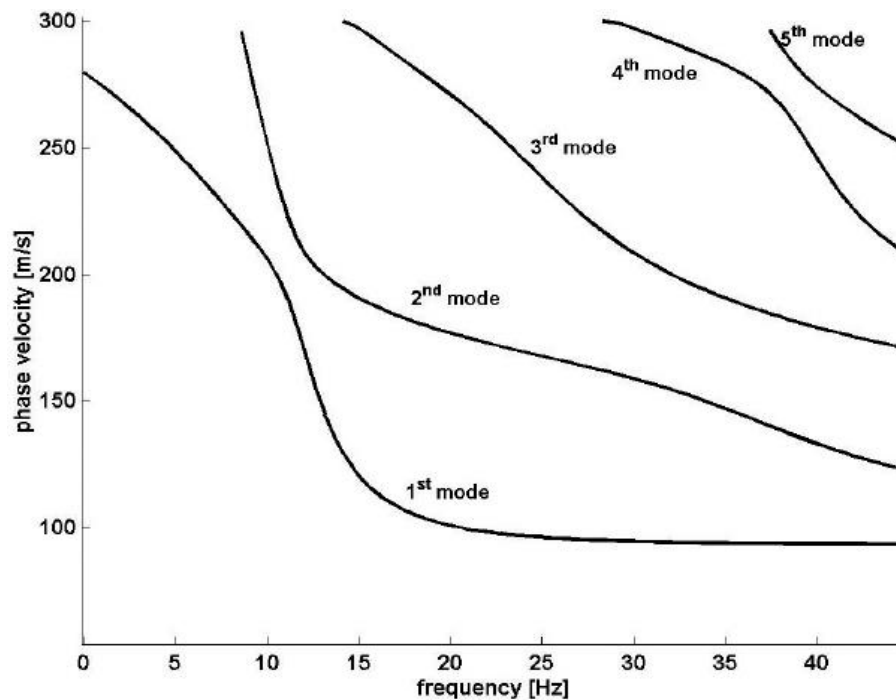


Figure 2.5: An example of modal curves (Socco and Strobbia, 2004)

2.3 Surface Wave Tomography

Surface wave tomography has been widely used as the major tool for the earth crust exploration on regional and global scales (Woodhouse and Dziewonski, 1984; Shapiro et al., 2004; Kugler et al., 2007; Moschetti et al., 2007; Villasenor et al., 2007; Yao et al., 2008; Zheng et al., 2008; Boiero, 2009; Li et al., 2009; Picozzi et al., 2009; Feng and An, 2010; Iglesias et al., 2010; Yao et al., 2010; Bao et al., 2015; Kästle et al., 2018; Fu et al., 2019).

On the global scale, surface waves generated by earthquakes are recorded by large networks of very low-frequency seismometers, processed and inverted for 3D velocity models. In recent years, many active and passive surface wave tomography applications in regional scale and for shallower targets have been documented. Contrary to the more classical MASW, where the DCs are obtained from a set of seismic traces recorded along a line, in SW tomography receiver pairs in line with a

source are used to estimate the average slowness DC along the path between the receivers. The DCs are then inverted to obtain velocity models using different inversion strategies.

Kugler et al. (2007) applied the surface (Scholte) wave tomography to determine a 3D in situ VS of the shallow-water marine sediments in northern Germany using air-gun source and recording the data by ocean-bottom seismometers.

Yao et al. (2008) applied surface wave tomography to ambient noise by using 25 temporary stations in southeast Tibet. Li et al. (2009) performed ambient noise Rayleigh wave tomography in western Sichuan and eastern Tibet and were able to show the spatial variations of low-velocity layers due to dense station coverage which was not possible in previous studies. Boiero (2009) determined the 3-D VS variations in the crust and upper mantle in the south-eastern borderland of the Tibetan Plateau, SW China, using the interstation Rayleigh wave phase velocity dispersion measurements from ambient noise and two-station analysis. Yao (2012) obtained a high-resolution lithospheric structure in SE Tibet by applying ambient noise and earthquake surface wave tomography thanks to the great improvements in data coverage by using dense portable array stations deployed in SE Tibet: He combined ambient noise and earthquake surface wave tomography, at overlapping periods, to average the phase velocity measurement for each two-station path: this increases the number of ray paths and reduces the error. Bao et al. (2015) applied surface wave tomography to ambient noise and earthquake data accumulated over the past decade. The extensive data allowed them to construct a high-resolution lithospheric VS model for Mainland China and adjacent. 1315 seismic stations were used to acquire the data: the largest number used up to that date.

Kästel et al. (2018) applied surface wave tomography to obtain a high-resolution 3-D model of seismic VS for the shallow crust and sedimentary basins below the Alps using ambient noise and earthquake phase velocity measurements using 313 stations for ambient noise and 387 stations for earthquakes. For the ambient noise, multi-

component receivers were used to record vertical, horizontal and transversal displacements which allowed them to obtain both Rayleigh and Love waves.

In this study, we apply surface wave tomography to a dataset acquired along a line and not over an area. The main task is to assess the feasibility of using ground roll present in hydrocarbon exploration data to obtain high-resolution 2D VS model of the near-surface.

2.3.1 Data acquisition

The data to be processed and inverted should have a high signal to noise ratio S/N over a wide frequency band. If it is not the case, stacking can be applied in order to increase S/N. The receiver spacing as well as the sampling rate should be short enough to avoid spatial and temporal aliasing. The source (Vibroiseis) is aligned with the two receivers (geophones) that must be spaced by, at least, half of the dominant wavelength to make reliable measurements (Yao et al., 2006). Each dataset has an optimal offset range between the source and the receivers, hence, datasets with too short or too long receiver spacing are not suitable for two-station tomography. The data used for SW tomography can be acquired from seismic data or SW data. When using seismic data which are not acquired on purpose for SW retrieval, the data quality might not be optimal. Even if space and time sampling are acceptable and source are usually powerful enough, the data might be band limited by the used sources and receivers. Moreover, the use of receiver groups (on purpose designed to directly filter the surface wave out), may reduce the surface wave band further which makes the data challengeable to work with.

2.3.2 Processing

In the processing step, multiple DCs are estimated from the raw data to provide the inputs for the inversion.

Figure 2.6 shows the processing workflow to extract the DCs. The first step is to choose the source shot and the receiver pair. Once they are chosen, the velocities at which

the envelope (group of waves) travels through a medium, called group velocities are picked from a spectrum for both traces 1 and 2. After picking the group velocities, the traces are windowed using a time window, according to the group arrival time at frequency of interest to eliminate unwanted events in the signal (noise, body waves, higher modes of surface waves) (Yao et al., 2005). After time windowing, the picked group velocities are cross-correlated to obtain the phase velocity dispersion for the receiver pair. The same process is applied for different sources and receiver pairs until enough DCs are obtained to cover the whole seismic line.

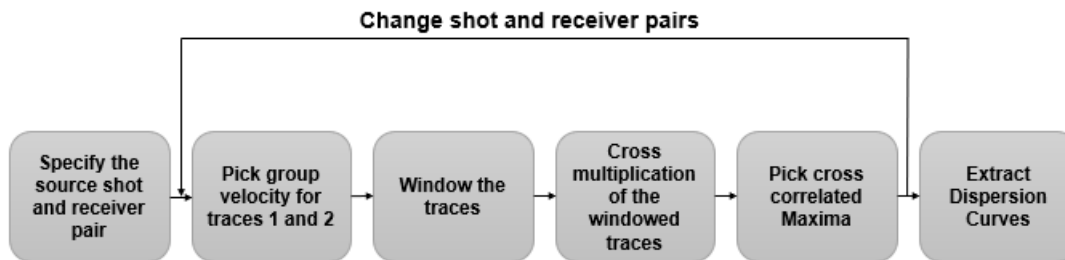


Figure 2.6: Workflow diagram of the process applied to extract the DCs.

2.3.2.1 Group velocities and time windowing

The group velocities are computed for both traces. The processing workflow is based on Dziewonski et al. (1969):

- I. A series of gaussian narrow band-pass filters, centered around the frequencies of interest is applied to the input seismogram $s(t)$ to filter it, the output is a series of filtered signals $a_f(t)$ where f is the central frequency of the band pass filter.
- II. The relevant quadrature signal $q_f(t)$ is computed for each filtered signal $a_f(t)$.
- III. The envelope of input seismogram $s(t)$ for frequency f is then $A_f(t) = (a_f(t)^2 + q_f(t)^2)^{1/2}$.
- IV. $A_f(t)$ is transformed into a function of group velocity $E_f(v_g)$, $A_f(t') = E_f\left(\frac{\Delta x}{t'}\right)$ where, v_g is the group velocity and Δx is the offset.

The computed group velocities are used to design a time window in order to isolate the fundamental mode. The time window is a cosine shoulder (Yao et al., 2005) centered at the group arrival time at frequency of interest $\omega(t, f_c)$ (equation 2.1) to eliminate unwanted events in the signal.

$$\omega(t, f_c) = \begin{cases} 1 & \text{if } t_g(f_c) - \frac{n}{f_c} < t < t_g(f_c) + \frac{n}{f_c} \\ \cos\left(\pi \frac{|t - t_g(f_c)| + \frac{n}{f_c}}{\frac{1}{f_c}}\right) & \text{if } -\frac{2}{f_c} < |t - t_g(f_c)| < \frac{2}{f_c} \\ 0 & \text{elsewhere} \end{cases} \quad (2.1)$$

where f_c is the frequency of interest, $t_g(f_c)$ is the arrival time of the group arrival time for the frequency of interest and n is a window constant with typical value 2-3. The optimal width and size of the window is determined through a series of tests (Da Col, 2013).

2.3.2.2 Cross-correlation and phase velocity computation

Each window applied on the seismograms is centered at the group delay time corresponding to the frequency (period) of interest. If we are using noise-free data, the windowing step can be skipped but in the data we worked on, it was an essential step to window the traces in order to remove unwanted events such as noise and higher modes.

After windowing the traces, they are cross-multiplied (Bloch and Hales, 1968), and the time delay should correspond to the travel time of the wave from one receiver to the other.

The cross-correlation matrix obtained is used to estimate the average slowness DCs along the path between the two receivers. After cross-correlation of the windowed traces, the cross-correlated maxima are picked, and the DC is obtained. The process is repeated for several sources and receivers configuration to obtain high data coverage.

2.3.3 Inversion

The last step of the surface wave tomography is the inversion. In this step, the goal is to estimate the mechanical properties (VS, VP and Poisson ratio) of the subsurface. The surface waves have high sensitivity to VS and lower sensitivity to VP and density (Foti et al., 2018). We assume the density and VP *a priori* so we only invert for the VS. Before dealing with the inversion algorithm we must solve the forward problem. The forward problem involves calculating the responses under the assumption that the physical properties of the earth are known. The experimental data gathered at a site are compared to simulated data until a satisfactory match is reached (Socco and Strobbia, 2004).

The forward and inversion algorithms used in this thesis are developed based on a code implemented by Boiero and illustrated in his Ph.D. thesis (Boiero, 2009) and modified by Da Col (2013) to make it suitable for exploration scale.

2.3.3.1 Forward Problem

The first step in the forward problem is to discretize the surface of the earth (x,y) using a grid of k points. At each point of the grid, a 1D VS model is considered. The travel time along a specified path AB is calculated according to the equation:

$$t_{AB}(\omega) = \int_A^B p(l, \omega) dl = \sum_{i=1}^I p_i(l_{AB}, \omega) dl_i, \quad (2.2)$$

where ω is the angular frequency, $p_i(l_{AB}, \omega)$ is the phase slowness for each path segment dl_i , along AB (with $\sum dl_i = l_{AB}$). In a general case, the phase slowness at any point i along AB is calculated by four surrounding points using bilinear interpolation as shown in figure 2.7. In case of 2D surface wave tomography, the interpolation is performed using the two closest grids from the point of the discretized path. The slowness at each grid point is computed using the model parameters of the 1D model and using Haskell (1953) and Thompson (1950) method, developed by Maraschini (2008) in MATLAB.

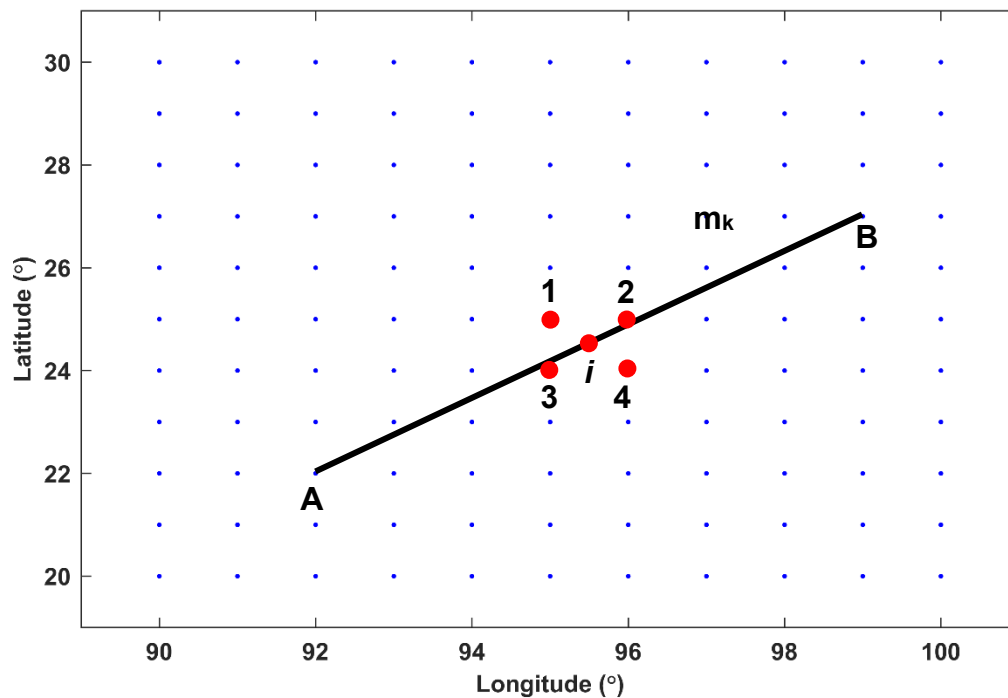


Figure 2.7: The solid line represents the path of the circle propagation between two stations A and B. The phase slowness p_i at any point i along a path is determined from the values at four surrounding points.

The slowness along path AB is estimated according to equation 2.3:

$$p_{AB}(\omega) = \frac{\sum_{i=1}^l p_i(l_{AB}, \omega) dl_{AB}}{l_{AB}} \quad (2.3)$$

The relative average velocity DC $c(\omega)$ between A and B is then:

$$c_{AB}(\omega) = \frac{l_{AB}}{t_{AB}(\omega)} = \frac{1}{p_{AB}(\omega)} \quad (2.4)$$

2.3.3.2 Inversion Algorithm

The inversion algorithm, implemented by Boiero (2009), employs a weighted least square method to iteratively update the initial model. It inverts the average slowness dispersion data \mathbf{p}_{obs} for K parameters ($\mathbf{k}=1, \dots, K$) where $\mathbf{m} = \mathbf{m}_k$ are the models parameters. The purpose is to minimize the objective function Q :

$$Q = \left[(\mathbf{p}_{obs} - p(\mathbf{m}))^T \mathbf{C}_{obs}^{-1} (\mathbf{p}_{obs} - p(\mathbf{m})) \right] + \left[(-\mathbf{R}_p \mathbf{m})^T \mathbf{C}_{Rp}^{-1} (-\mathbf{R}_p \mathbf{m}) \right] \quad (2.5)$$

where, $p(\mathbf{m})$ is the phase slowness along each path. \mathbf{C}_{obs} is the covariance of the observed data, while the covariance \mathbf{C}_{Rp} contains the strength of the lateral constraints and depends on the expected variability of different models \mathbf{m} . \mathbf{R}_p is the regularization matrix that relates m_k to models at nearby points. It contains 3 different numbers: -1, 0 and 1. -1 and 1 are for the constrained parameters and 0 elsewhere.

$$\mathbf{R}_p = \begin{pmatrix} 1 & 0 & \dots & 0 & -1 & 0 & \dots & 0 & 0 & 0 \\ 0 & 1 & 0 & \dots & 0 & -1 & 0 & \dots & 0 & 0 \\ 0 & 0 & 1 & \dots & 0 & 0 & -1 & \dots & 0 & 0 \\ \vdots & \vdots & \vdots & \ddots & \vdots & \vdots & \vdots & \ddots & \vdots & \vdots \\ 0 & 0 & 0 & \dots & 1 & 0 & 0 & \dots & -1 & 0 \\ 0 & 0 & 0 & \dots & 0 & 1 & 0 & \dots & 0 & -1 \end{pmatrix} \quad (2.6)$$

This regularization matrix causes an improvement in the conditions and keeps the propagation error under control which will reduce the misfit function Q . On the other hand, if it is excessive or only chosen by mathematical arguments, the solution loses connection to the real data (e.g. Tarantola, 2005). \mathbf{R}_p helps to minimize the differences between the model m_k and the models at surrounding points. Its effectiveness depends on \mathbf{C}_{Rp} (Auken and Christiansen, 2004). The effect of \mathbf{C}_{Rp} on the inversion result can be determined by calculating the residual in equation 2.7:

$$\mathbf{R} = \mathbf{p}_{obs} - p(\mathbf{m}_{end}) \quad (2.7)$$

Where \mathbf{m}_{end} is the final inversion model. Excessive regularization leads to unrealistic smoothing of model parameters which increases the residuals (Boiero and Socco, 2010). To minimize Q , at the n^{th} iteration, the model solution is expressed as:

$$\mathbf{m}_{n+1} = \mathbf{m}_n + \left[\begin{array}{c} (\mathbf{G}^T \mathbf{C}_{obs}^{-1} \mathbf{G} + \mathbf{R}_p^T \mathbf{C}_{Rp}^{-1} \mathbf{R}_p + \lambda \mathbf{I})^{-1} \times \\ (\mathbf{G}^T \mathbf{C}_{obs}^{-1} (\mathbf{p}_{obs} - p(\mathbf{m}_n)) + \mathbf{R}_p^T \mathbf{C}_{Rp}^{-1} (-\mathbf{R}_p \mathbf{m}_n)) \end{array} \right] \quad (2.8)$$

where λ is the Marquart damping parameter (Marquart, 1963). The sensitivity of dispersion slowness p_k to model parameters m_k is described by the Jacobian sensitivity matrix G :

$$G = \begin{pmatrix} \dots & \dots & \dots & \dots & \dots & \dots & \dots \\ \dots & \frac{\partial p_{AB}}{\partial m_1} & \frac{\partial p_{AB}}{\partial m_2} & \dots & \frac{\partial p_{AB}}{\partial m_4} & \frac{\partial p_{AB}}{\partial m_3} & \dots \\ \dots & \dots & \dots & \dots & \dots & \dots & \dots \\ \dots & \frac{\partial p_{CD}}{\partial m_1} & \frac{\partial p_{CD}}{\partial m_2} & \dots & \frac{\partial p_{CD}}{\partial m_4} & \frac{\partial p_{CD}}{\partial m_3} & \dots \\ \dots & \frac{\partial p_{EF}}{\partial m_1} & \frac{\partial p_{EF}}{\partial m_2} & \dots & \frac{\partial p_{EF}}{\partial m_4} & \frac{\partial p_{EF}}{\partial m_3} & \dots \\ \dots & \dots & \dots & \dots & \dots & \dots & \dots \end{pmatrix} \quad (2.9)$$

where each element of the sensitivity matrix G is expressed as:

$$\frac{\partial p_{AB}(\omega)}{\partial m_k} = (f_k)_{AB} \times \frac{\partial p_k(\omega)}{\partial m_k} \quad (2.10)$$

2.4 Checkerboard Test

The checkerboard test is useful to assess the ability of tomographic inversion to resolve structural details in the earth by testing it on a ‘synthetic’ dataset (Da Col, 2013). The checkerboard test can be applied to any inversion procedure without knowing the internal operation of the inversion, it gives a general picture of the resolving power of a tomographic inversion.

An initial 1D VS model is perturbed to create canvas of alternated positive and negative perturbed stripes (Papadopoulou et al., 2019). The synthetic travel times to all receivers from all sources used in the original tomographic inversion are computed by

the forward modelling, and then the synthetic travel times (as DCs) are inverted in the same manner as the actual data. The inversion results are compared to the true model and the resolution is indicated by the accuracy with which the stripes are detected. An example of the perturbation scheme applied to the initial model is given in figure 2.8, where the black and white tiles show a negative and a positive perturbation applied to two model points by two layers, respectively.

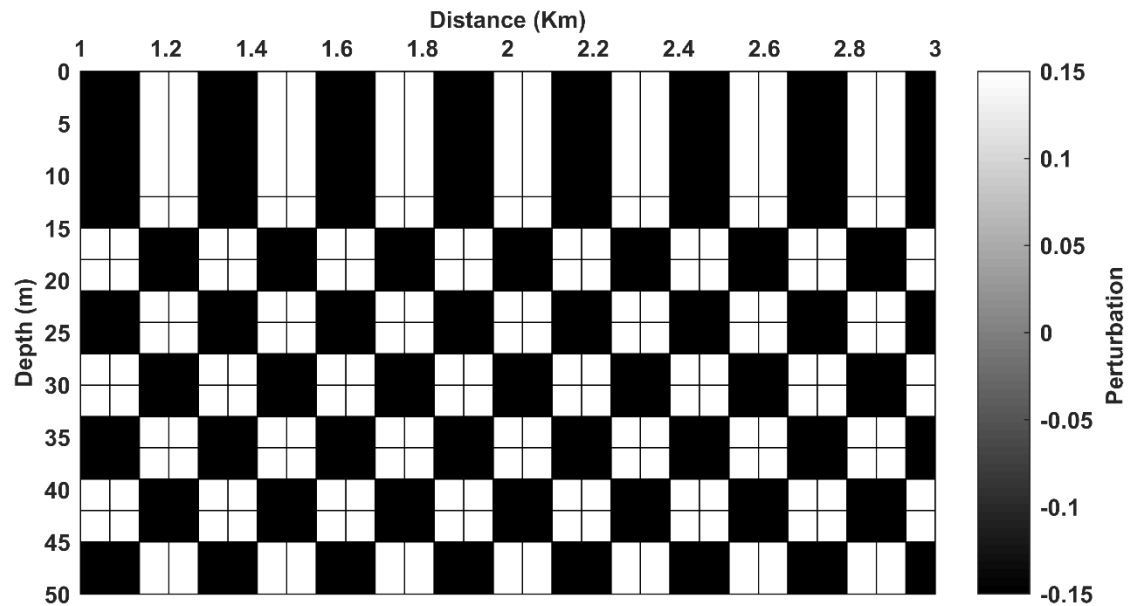


Figure 2.8: Scheme of positive and negative 15 percent perturbation.

Chapter 3: Data, Processing and Results

In this chapter, we will describe the dataset and the acquisition layout. Then, we will present the selection of the receiver pairs, the processing used to extract the DCs and the inversion of the retrieved DCs to obtain 2D VS models. Finally, a checkerboard test is performed to evaluate the tomographic inversions.

3.1 Data

3.1.1 Test site

The dataset consists of a single land seismic line of 12 km. The data, provided by Total E&P, and the location of this dataset, as well as its name, will not be revealed for confidentiality reasons. The acquisition line is deployed along a hillslope and crosses some alluvial fans that create low-velocity zones on top of the sedimentary rocks and thus the need of characterization of the near-surface velocity. A scheme of this seismic line is given in figure 3.1.

According to previous studies, VP for the first 200 m ranges between 2500 m/s to 3500 m/s which is considered a high velocity for near-surface (Masoni, 2016).

The total number of receiver groups along the line is 601 evenly spaced along 12 km which means that the spacing between the receivers is 20 m. The variation of the topography is relatively low in this portion. Each receiver group consists of 12 vertical geophones of 10 Hz natural frequency spaced 1.66 m. The number of source points is 600 evenly spaced with spacing equal to 20 m. The source is a Vibroseis. At each source position, four sweeps that have a frequency band of 4 Hz to 90 Hz were recorded separately by all receivers and then stacked.

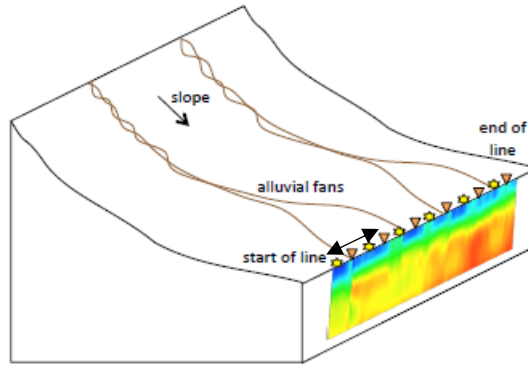


Figure 3.1: A scheme of the location where the dataset was acquired along a seismic line (modified from Masoni, 2016). The black double arrow shows the portion of the line in which the data were processed in the present work.

Many analyses have been carried on the same dataset. Masoni (2016) applied surface wave 1D inversion (SWODI) to obtain shear and compressional wave velocity sections. Karimpour (2018) applied a processing workflow and quality control on the data and obtained an optimal range for the offset in the multi-station method. Khosro Anjom et al. (2019) performed surface wave direct transform on the dataset to obtain shear and compressional wave velocity sections. This study includes 200 shots and 101 receivers where the receivers are in between the shots leaving 50 shots on each side. The receiver array covers 2 km out of the 4 km as shown in figure 3.2. Here, first, we process the data using two-station method, and, then, we apply a tomographic inversion to obtain a 2D VS section of the subsurface.

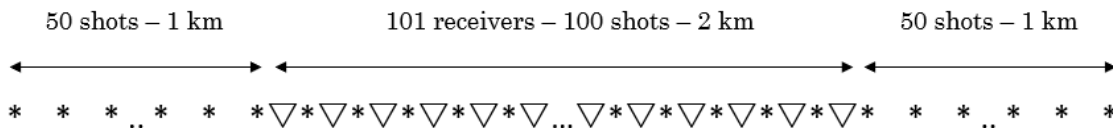


Figure 3.2: Scheme showing the configuration of sources and receivers along the analyzed 4 km (▽-receivers, * - shots).

3.2 Processing

Before applying the processing workflow outlined in chapter 2 (figure 2.6), several tests were carried to find the optimal processing parameters and select the best shot and receiver couples configuration (Appendix A). The optimal offsets between the source and the two receivers were investigated according to the quality of the obtained DC and its frequency bandwidth. According to the test results (Appendix A), the optimal offset between the source and the first receiver is 150 m for this dataset. On the other hand, in Appendix A, the distance between the two receivers were optimized considering the half-wavelength criterion described in Yao et al. (2006). Yao et al. (2006) showed that the maximum wavelength that can be retrieved in the two-station method is twice the distance between the receivers. So, the distance between the two receivers should be at least half the maximum desirable wavelength. According to this criterion and considering the tests in Appendix A, we use receiver couples with distance ranging from 60 m to 140 m.

The source shots and receiver couples used to obtain the DCs are shown in table 3.1 where for each shot the first receiver is 150 m from the source while the second receiver is between 60 m to 140 m from the first receiver. The sources, except for the last (shot number 156), are on one side of the receivers. Only one source was used for each receiver pair, hence, no stacking is applied.

Shot number (150 m from the first receiver)	Receiver pairs				
	60 m spacing	80 m spacing	100 m spacing	120 m spacing	140 m spacing
42	1&4	1&5	1&6	1&7	1&8
44	3&6	3&7	3&8	3&9	3&10
46	5&8	5&9	5&10	5&11	5&12
48	7&10	7&11	7&12	7&13	7&14
⋮	⋮	⋮	⋮	⋮	⋮
132	91&94	91&95	91&96	91&97	91&98
134	93&96	93&97	93&98	93&99	93&100
156	100&97	100&96	100&95	100&94	100&93

Table 3.1: Receiver pairs used for each shot.

Following the processing workflow explained in chapter 2 (figure 2.6), we compute a DC corresponding to each path in table 3.1. First, we compute the group velocity corresponding to each trace. After computing group velocity for each receiver, we window the traces. Then, we compute the corresponding cross-multiplication matrix and we pick the DC. Consequently, for each shot, we estimate 5 DCs using different locations for the second receiver. This processing setting is repeated every 40 m to have enough coverage and cross-paths for the surface wave tomography. To improve the coverage at the end of the receiver line, we use a single shot from the other side of the receiver line (shot 156). The total number of paths analyzed is 240.

3.2.1 Processing example

The following example shows the processing workflow applied for source number 50 and receiver pair 9 and 16. Figure 3.3a and figure 3.4a show the spectrum of: a) the picked group velocity against frequency for traces 1 and 2, respectively. In figure 3.3b and 3.4b, for the same traces, we show the time frequency spectrum.

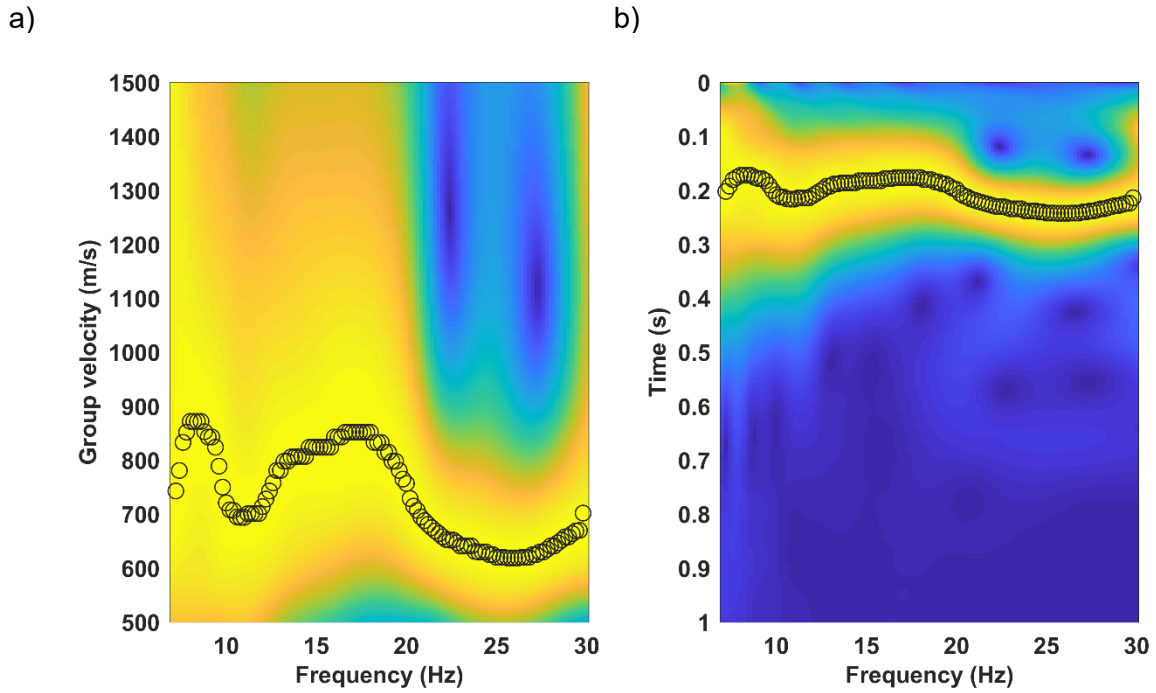


Figure 3.3: Computed spectrum of the first receiver: a) picked group velocity vs frequency and b) time vs frequency.

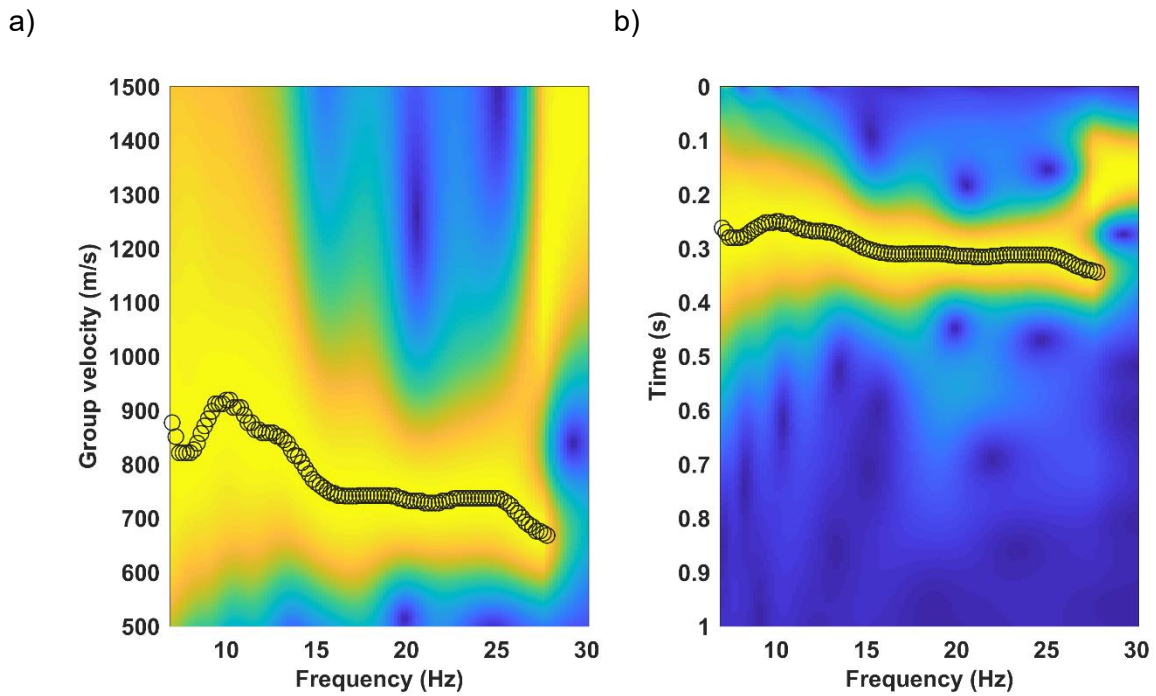


Figure 3.4: Computed spectrum of the second receiver: a) picked group velocity vs frequency and b) time vs frequency.

After picking the group velocities for both traces, they are windowed at the frequency of interest. Then, the windowed traces are cross-multiplied to obtain the cross-multiplication matrix shown in figure 3.5a. The DC corresponding to the path between the receiver is then estimated by picking the local maxima in the cross-multiplication matrix.

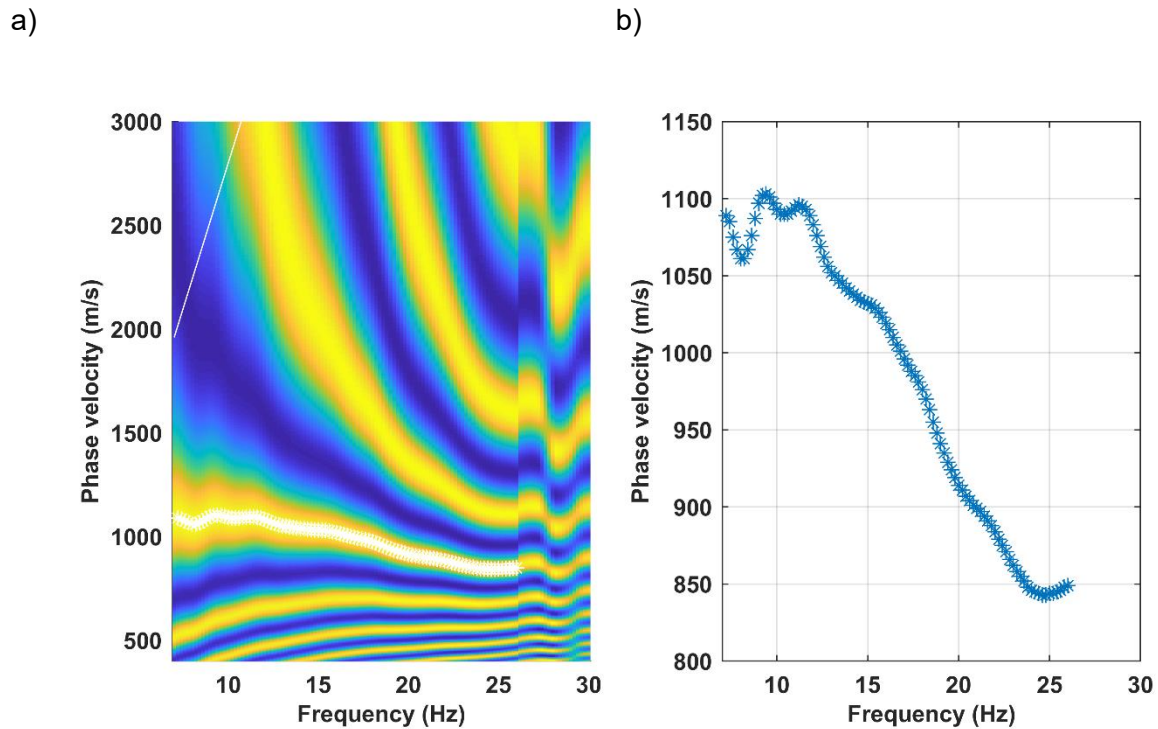


Figure 3.5: DC for shot number 50 and receiver pair 9&16: a) The cross multiplication matrix of the two traces b) Picked DC.

3.3 Results

3.3.1 Dispersion Curves

240 DCs corresponding to the defined paths were computed. The estimated DCs are plotted in figure 3.6. The average frequency range of the DCs is between 12 Hz and 24 Hz. There is a lack of information at low frequencies that reflect the deep portion of the subsurface. The minimum recovered frequency is 9 Hz while the maximum is 30 Hz.

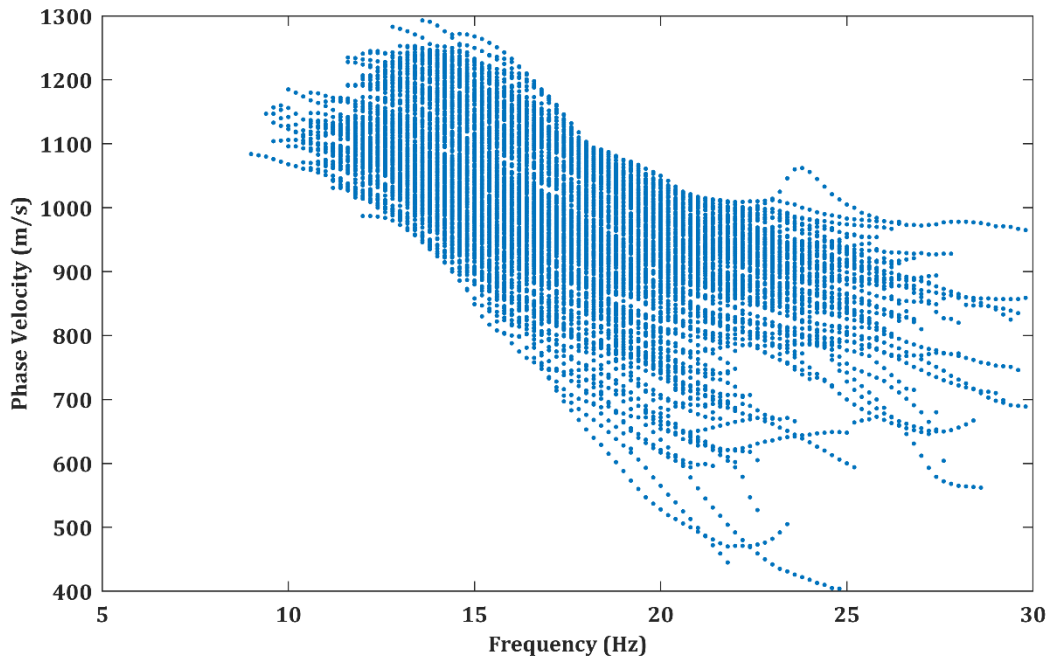


Figure 3.6: DCs plotted as phase velocity vs frequency.

Figure 3.6 is transformed into wavelength vs phase velocity (figure 3.7) by using the equation 3.1:

$$\lambda = \frac{V}{f}, \quad (3.1)$$

where λ is the wavelength in m, V is the phase velocity in m/s and f is the frequency in Hz. The minimum wavelength is around 20 m while the maximum is close to 120 m.

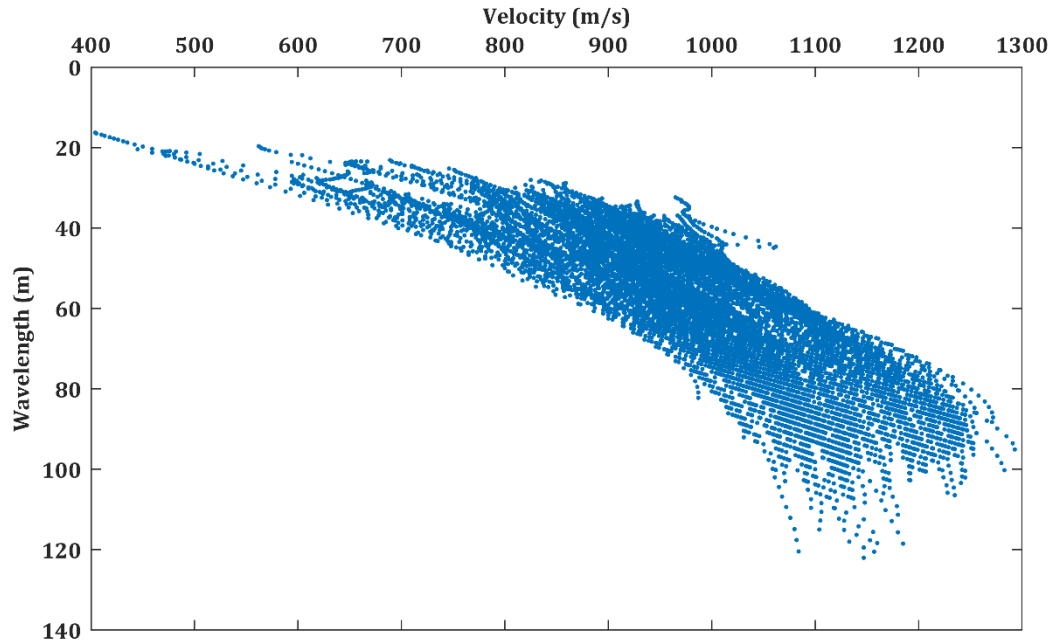


Figure 3.7: DCs plotted as wavelength vs phase velocity.

3.3.2 Coverage

The coverage is an important parameter for surface wave tomography that reflects the number of paths crossing each model point. Figure 3.8 shows the coverage in frequency domain at every position of the line.

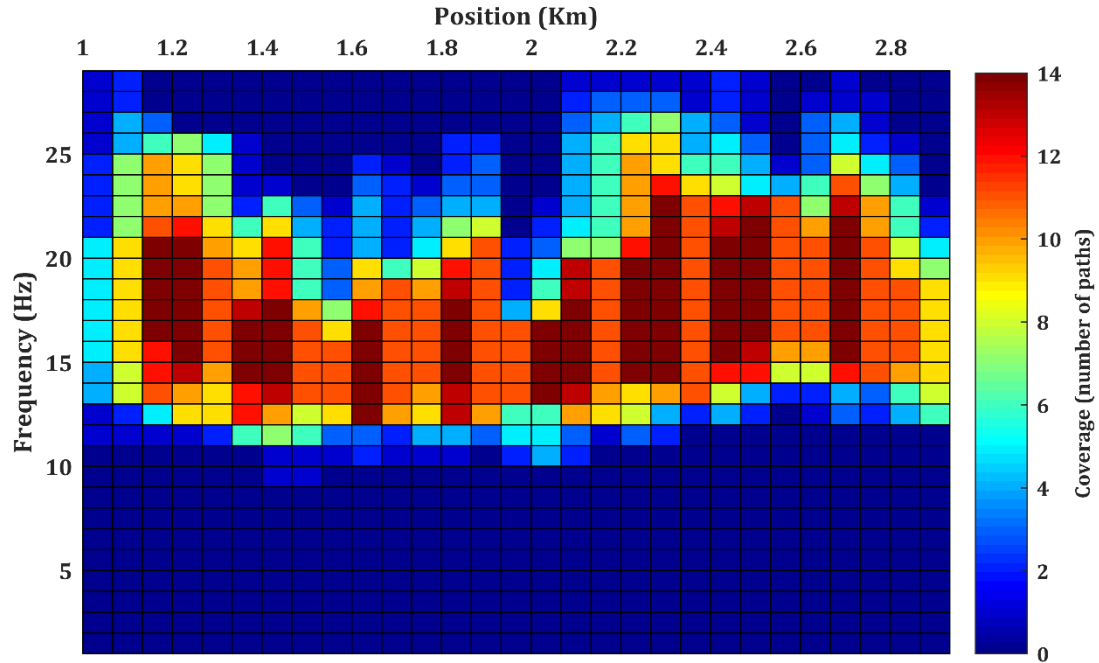


Figure 3.8: The coverage (number of paths) at the position of each model point shown at each frequency.

The colorbar indicates the coverage in number of paths at each point. There is no data coverage below 9 Hz. The first and the last 0.15 km of the seismic line (edges of the receivers line) have relatively low maximum coverage (5 to 9) compared to the rest of the line (11 to 14). At each model point, the coverage increases from the lowest frequency to reach a maximum in the middle of the frequency band then it decreases at high frequency to reach zero.

Using the DCs in terms of wavelength (figure 3.7), we computed the wavelength coverage. In figure 3.9, we show the coverage in wavelength domain where, similarly to figure 3.8, the colorbar shows the number of paths passing through a model point.

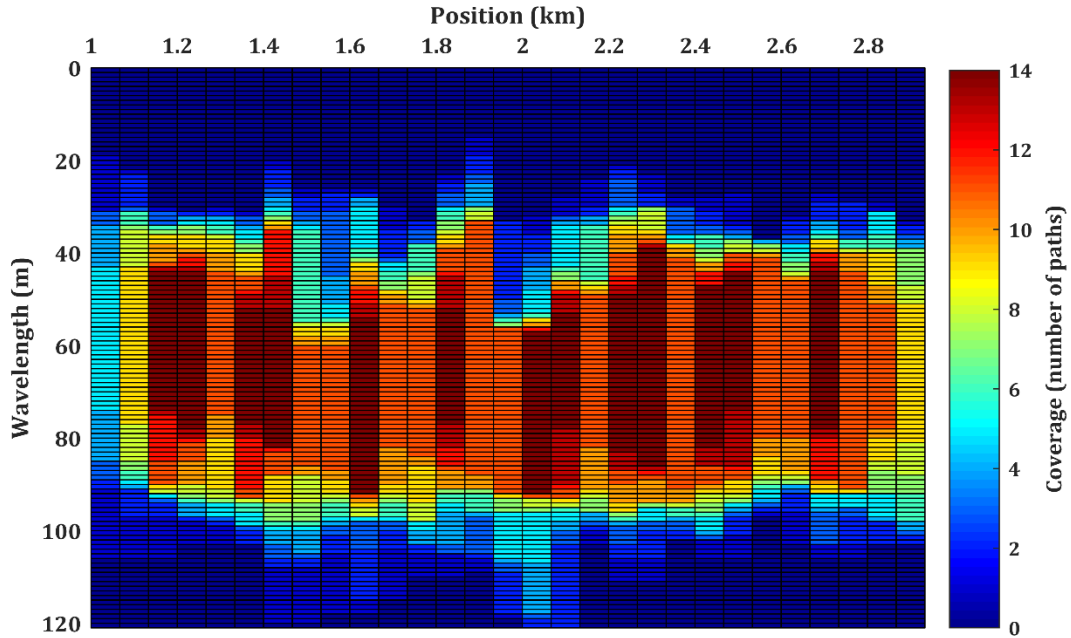


Figure 3.9: The coverage (number of paths) at the position of each model point shown at each wavelength.

Considering the rough assumption of the wavelength/2 for the depth conversion, the variations in the first 12 m of the subsurface cannot be recovered as there are a few DC points reflecting wavelength lower than 24 m. At the same time, the data coverage above 100 m of wavelength is reduced, significantly. So, similarly, it is unlikely for the surface wave tomography to recover reliable model beyond 50 m of investigation depth.

A novel method to represent the coverage in 2D is implemented in MATLAB. It consists of plotting each path between the receivers based on the average phase velocity of the path within its wavelength range. The aim of this method is to detect the lateral and horizontal variations from a phase velocity plot before performing the inversion. This will help in choosing the constraints to run the inversion. Figure 3.10 shows the 2D coverage plot corresponding to the receiver pairs chosen along a seismic line and its phase velocity in m/s.

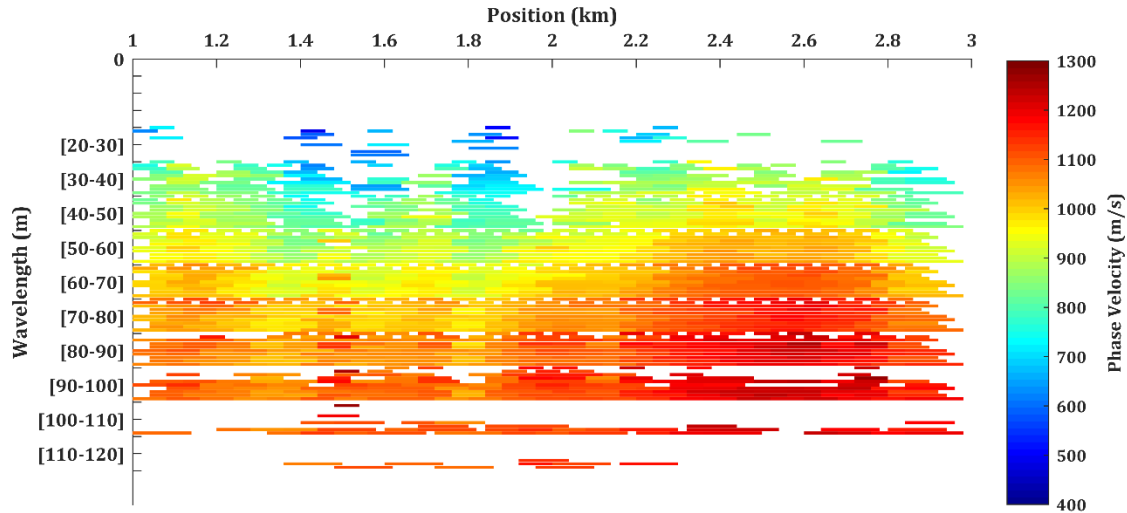


Figure 3.10: Representation of each path with a color that corresponds to the average phase velocity at the given wavelength.

Each line on the plot presents the length of the different paths joining the receiver pairs shown in table 3.1. The color scale is a range between the minimum and the maximum phase velocities retrieved for DCs. The figure shows a strong lateral discontinuity of phase velocities retrieved for DCs. The figure shows a strong lateral discontinuity of phase velocity at 2 km: there is an increase of the phase velocity starting from 2 km to 3 km compared to part from 1 km to 2 km. The coverage of the figure 3.9 matches with the coverage of figure 3.10, where both show a high coverage between 30 m and 100 m of wavelength.

3.3.3 Inversion

The choice for the inversion settings is optimized based on the coverage computed in the previous part. According to the coverage in figure 3.10, we performed multiple inversions with the same model parametrization (number of models, layers and investigation depth) with and without lateral constraints. Laterally constraint inversion (LCI) limits the solution non-uniqueness and provides smooth and reliable VS estimation where no strong lateral variation is present (Socco et al., 2009). Adding a lateral constraint to the inversion means that the neighboring 1D models are linked together and the velocity updates are constrained so that a more consistent VS model can be estimated. On the other hand, the use of strong lateral constraints can result in over-smoothing of the final model, and this can be evaluated by comparing the residual

misfit between the DC of the final and real model for the constrained and unconstrained inversions. Table 3.2 summarizes the inversions performed. 30 1D model points, evenly spaced, were defined along the 2 km line. The model consists of 12 layers above a half space, the first layer is 12 m thick while the other 11 layers are 3 m thick each, which makes the investigation depth of around 50 m. The first inversion was carried out without imposing any constraint. The second inversion had a horizontal constraint equal to 400 m/s. The third inversion had a horizontal constraint equal to 200 m/s while the fourth inversion had a horizontal constraint of 100 m/s. For the fifth inversion, we kept the same lateral constraint as in the fourth inversion (100 m/s) but we broke the constraint in the middle of the line because of the strong lateral variations shown in figure 3.10. For each inversion, an analysis of the residuals is performed to make sure the constraints are not too strong, and the estimated VS model is not over-smoothed. All the inversions are vertically unconstrained.

Inversion number	1	2	3	4 and 5
Settings				
Number of layers	12+half space	12+half space	12+half space	12+half space
Model points	30	30	30	30
Lateral constraints (m/s)	No Cons.	400	200	100
Model's length (km)	2	2	2	2

Table 3.2: The settings for each inversion.

For all inversions, the same initial model was used. The model parameters used are the density (1800 kg/m^3), Poisson ratio (0.33), number of layers (12 layers above half space) and the VS (1100 m/s). The VS of the initial model is shown in figure 3.11.

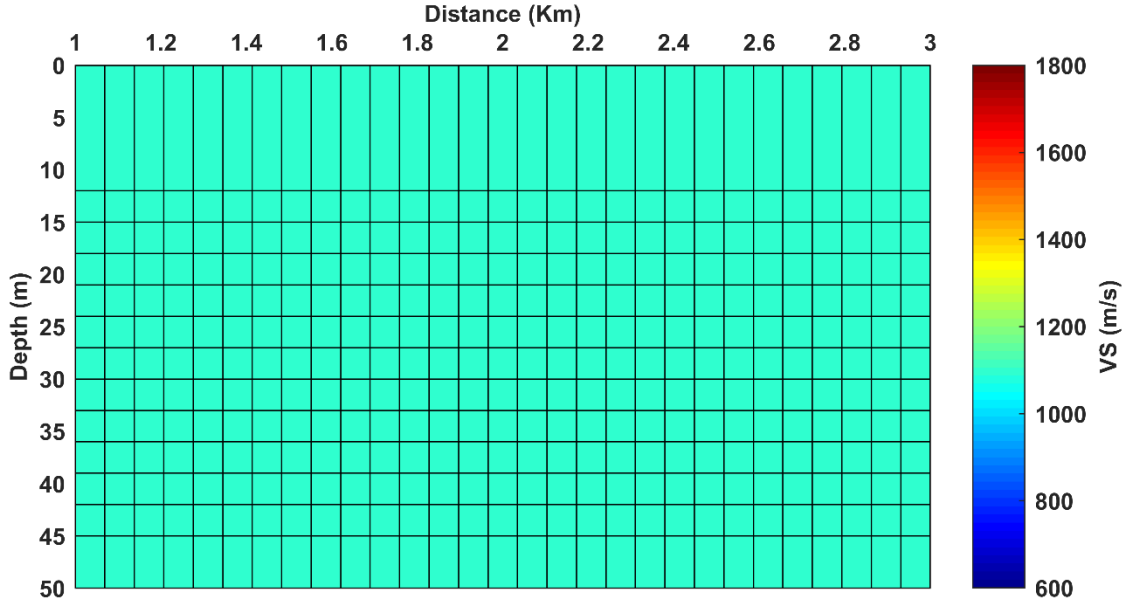


Figure 3.11: A homogeneous Initial model composed of 30 1D models and 12 layers above half space. The velocity of all layers is 1100 m/s.

3.3.3.1 Inversion 1: unconstrained

The VS result of the unconstrained inversion is shown in figure 3.12. The inversion shows strong VS variations: high and low velocity spots are visible along the line at different depths.

For each iteration, we calculate the global misfit between the inverted and the real DCs as:

$$Misfit_{Global} = \sqrt{\sum_{j=1}^K \sum_{i=1}^N \frac{(v_{exp,i} - v_{syn,i})^2}{e^2}} \quad (3.2)$$

where $v_{exp,i}$ is the experimental phase velocity at a specific frequency, $v_{syn,i}$ is the value of the computed synthetic phase velocity at the same frequency, e is the variance of the observed phase velocity, K is the number of paths and N is the number of frequency components of each path. In figure 3.13, we show the evolution of the global misfit corresponding to the unconstrained inversion shown in figure 3.12. The inversion routine automatically exits the loop when the global misfit reaches a local minima.

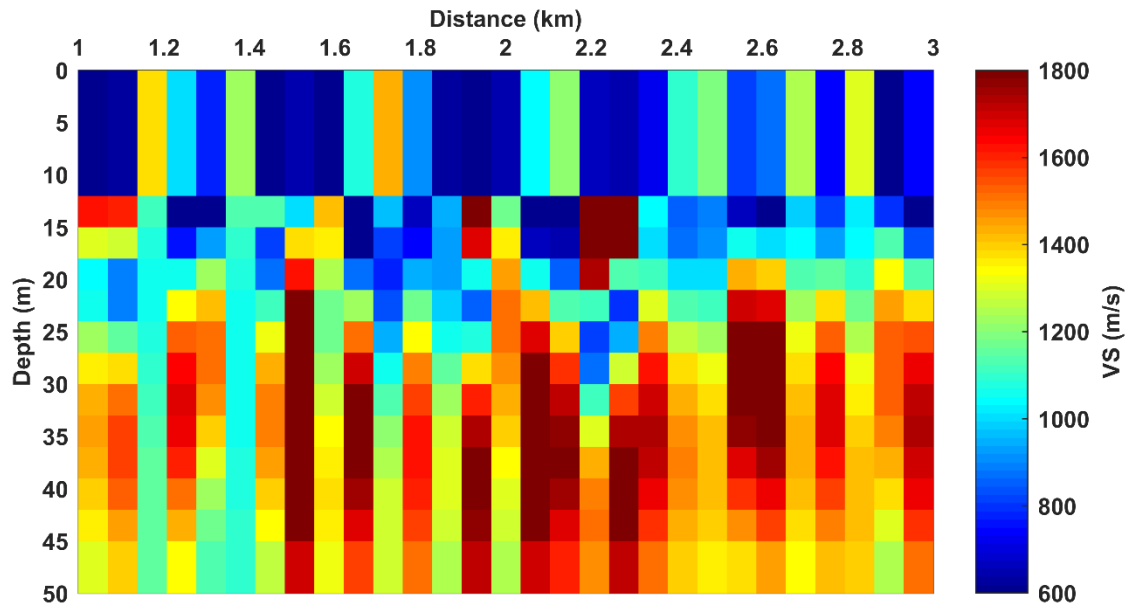


Figure 3.12: Inverted model for unconstrained inversion.

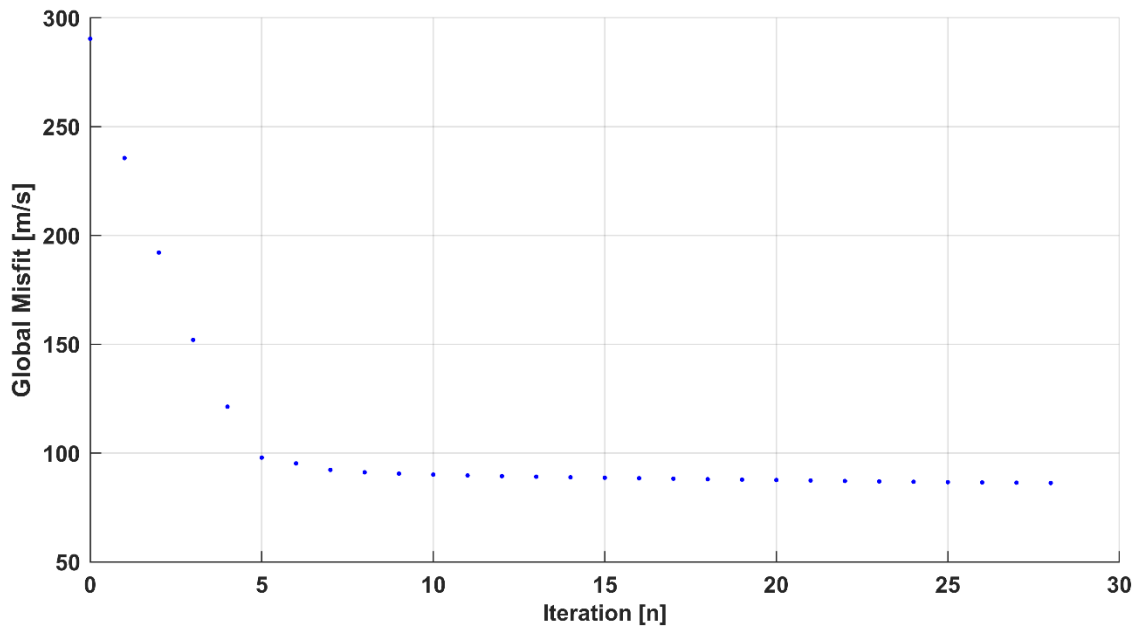


Figure 3.13: Misfit corresponding to the 1st inversion. 28 iterations needed to reach the lowest misfit.

The global misfit is equal to 86.3 m/s after 28 iterations.

The similar misfit can be defined for the DCs of individual paths as:

$$misfit = \sqrt{\sum_{i=1}^N \frac{(v_{exp,i} - v_{syn,i})^2}{e^2}} \quad (3.3)$$

In figure 3.14, we show the misfit of each DC (path) corresponding to the unconstrained inversion in figure 3.12. The highest and the lowest misfit (30.69 and 0.97) were registered for paths 51 and 193, respectively, and they are highlighted by a red circle. The DC of path 209 showed a low misfit (1.17) where it is highlighted in green. The DC of path number 220 with a misfit (4.76) is marked by a black circle. These paths are compared for all inversions to check the effect of increasing the lateral constraint on the misfit.

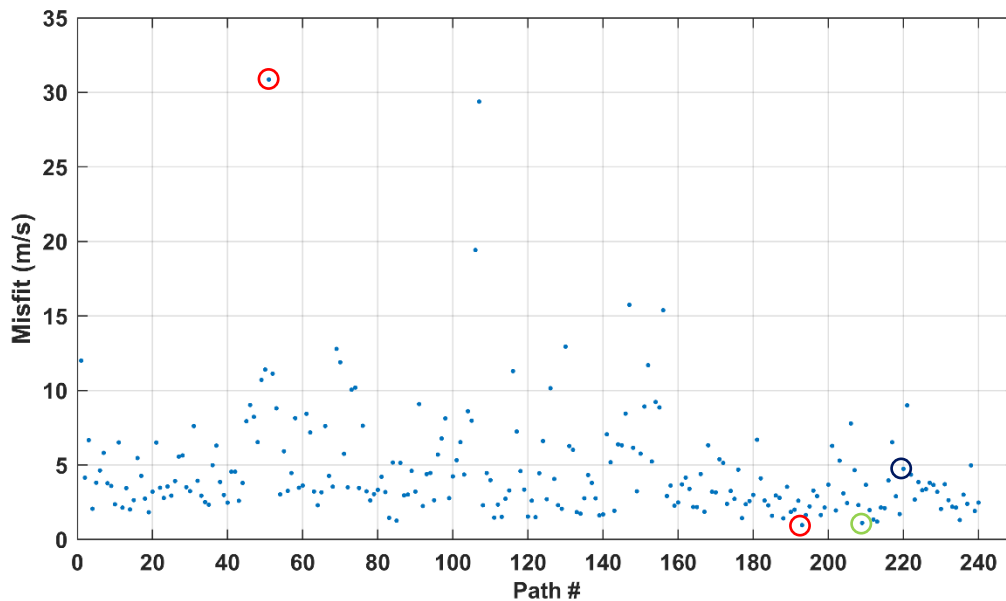


Figure 3.14: Misfit of the DCs of different paths for inversion 1.

3.3.3.2 Inversion 2: lateral constraint equal to 400 m/s

The second inversion is laterally constrained with a horizontal constraint equal to 400 m/s. The setting of the initial model is the same as the previous inversion as shown in figure 3.11. The inverted VS model is shown in figure 3.15. The model shows no significant changes with respect to the unconstrained inversion and presents all

previous sharp variations in VS estimation. The global misfit computed using equation 3.2 of each iteration (28 in total) is shown in figure 3.16. At the last iteration, it slightly increased to 86.5 m/s compared to unconstrained inversion.

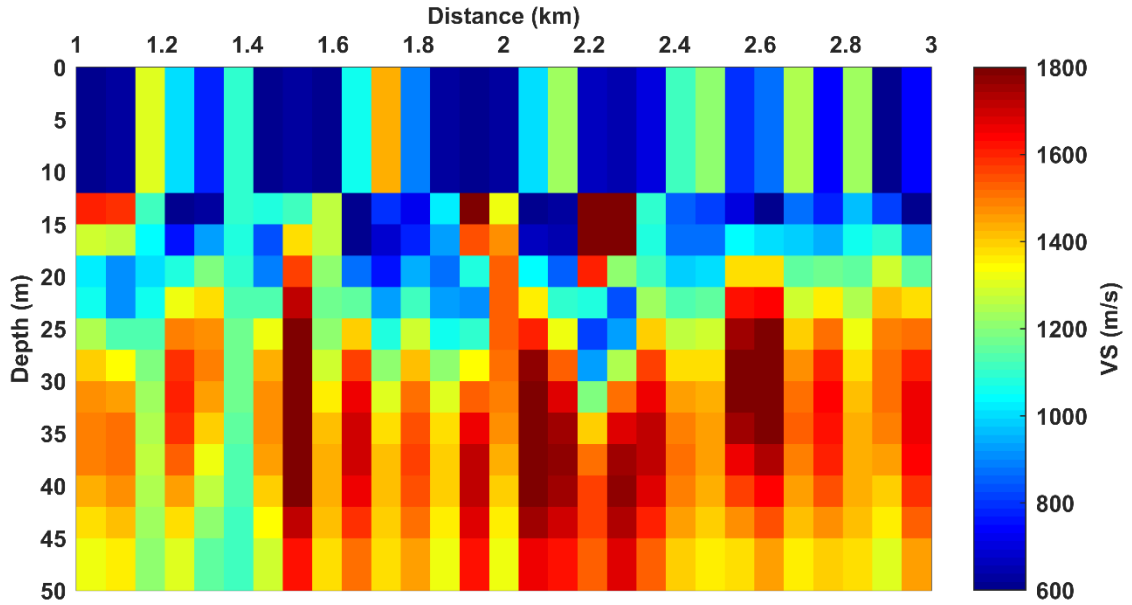


Figure 3.15: Inverted model for Inversion 2 (inversion parameters in table 3.2).

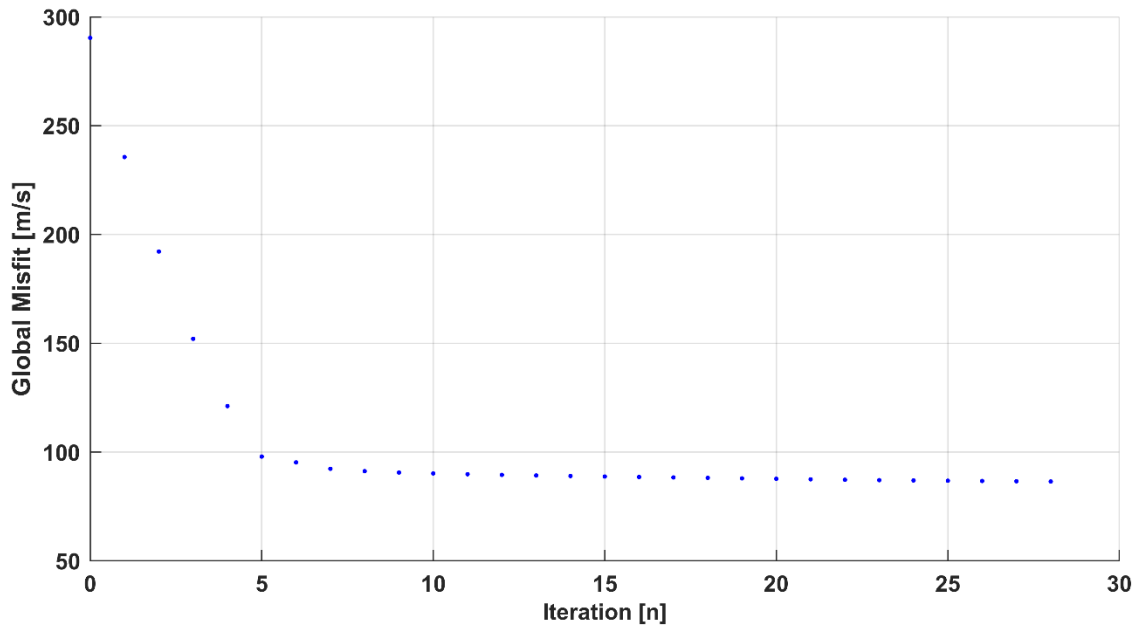


Figure 3.16: Misfit corresponding to the 2nd inversion. 28 iterations needed to reach the lowest misfit.

The misfit of each path is computed using equation 3.3 and shown in figure 3.17. Similarly to unconstrained inversion, the highest and lowest misfit corresponds to path 51 and 193 (30.86 and 0.97), respectively, which are highlighted in red. The paths 209 and 220 (misfit equal to 1.11 and 4.74 respectively) are also shown in green and black, respectively.

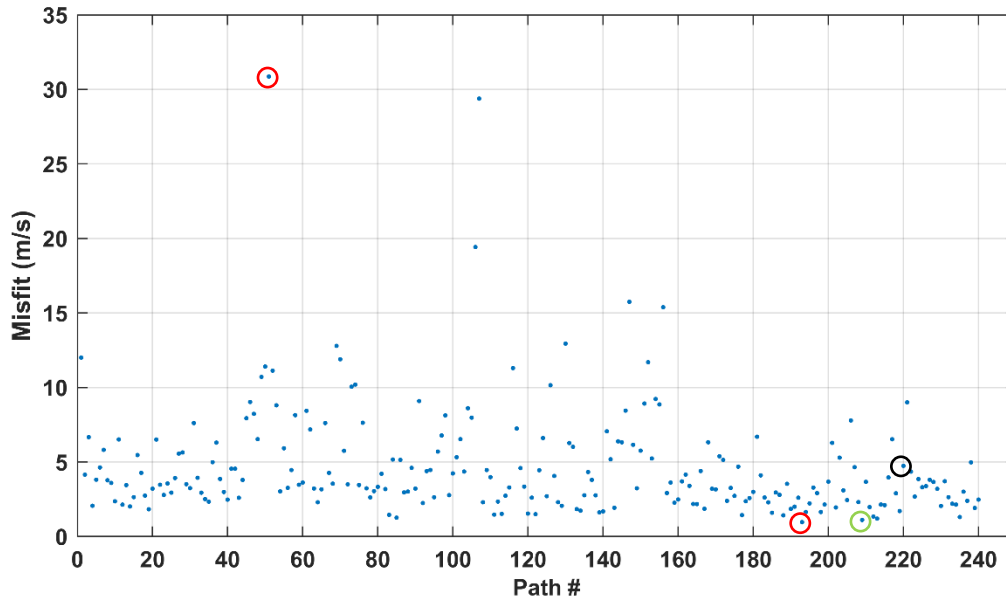


Figure 3.17: Misfit of the DCs of different paths for inversion 2.

3.3.3.3 Inversion 3: lateral constraint equal to 200 m/s

A stronger lateral constraint (200 m/s) is imposed for the third inversion. The setting of the initial reference model is the same as the previous inversion (homogeneous model shown in figure 3.11). The inverted model is shown in figure 3.18, where estimated VS model shows a smoother model with respect to inversion 1 and 2. However, the model still shows strong lateral variations. The global misfit, calculated using equation 3.2, is shown in figure 3.19. The last iteration shows similar misfit (87.1 m/s) compared to inversion 1 and 2 which suggests the lateral constraint is not over-smoothing the final result.

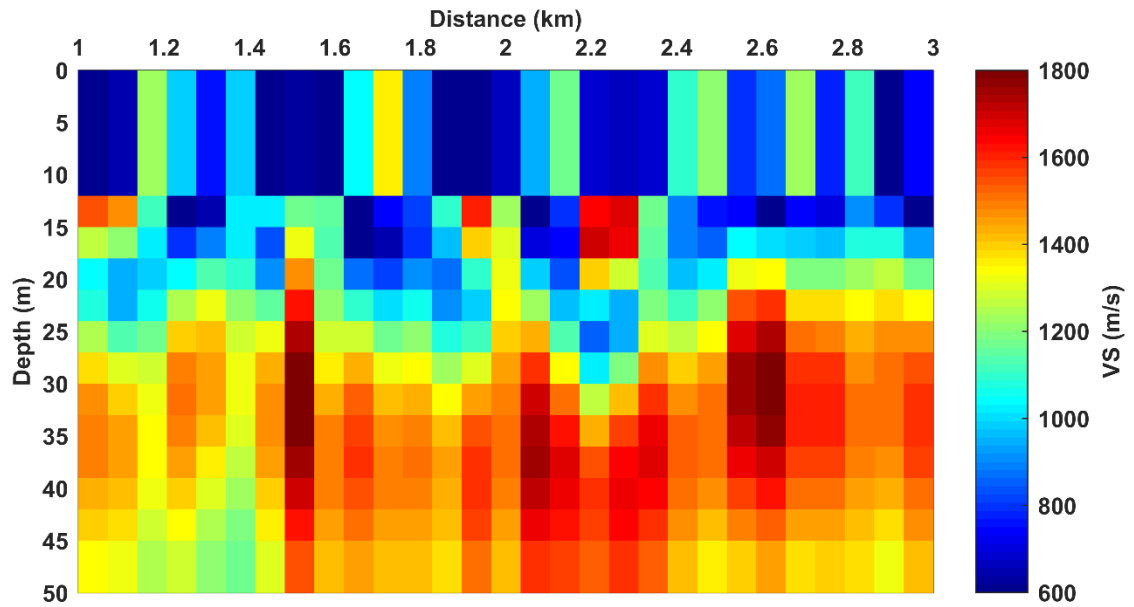


Figure 3.18: Inverted model for Inversion 3 (inversion parameters in table 3.2)

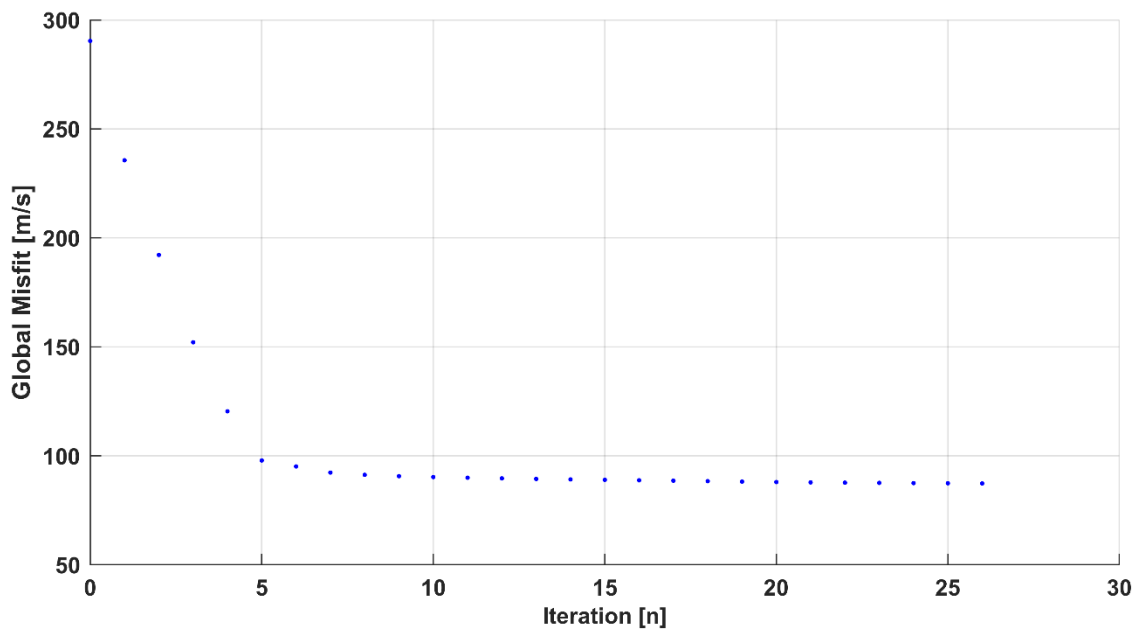


Figure 3.19: Misfit corresponding to the 3rd inversion. 26 iterations needed to reach the lowest misfit.

Figure 3.20 shows the misfit of each path for inversion 3. The highest and the lowest (31.14 and 0.97), corresponding to path numbers 51 and 193 respectively, are marked

by a red circle. The paths 209 and 220 (misfits equal to 1.09 and 4.71) are shown in green and black circles, respectively.

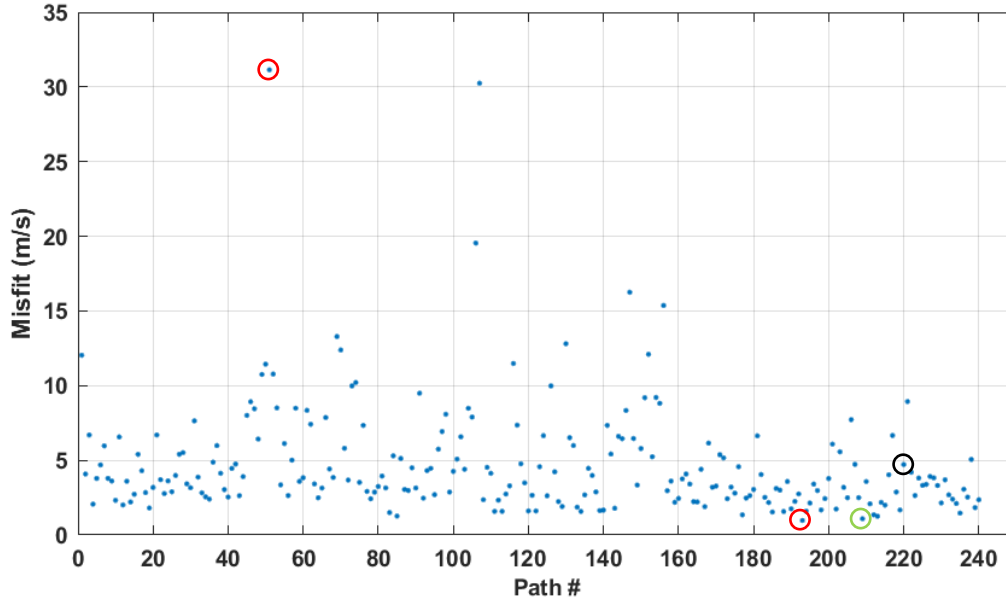


Figure 3.20: Misfit of the DCs of different paths for inversion 3.

3.3.3.4 Inversion 4: lateral constraint equal to 100 m/s

The previous laterally constrained inversions slightly improved the consistency and smoothness of the final model. In the fourth inversion, we use a stronger constraint (100 m/s) to further limit the lateral variation. As of before, we use the same homogeneous initial for the inversion (figure 3.11). The estimated VS model is shown in figure 3.21, the variation is smaller within the model and it shows a smoother result compared to the previous three inversions.

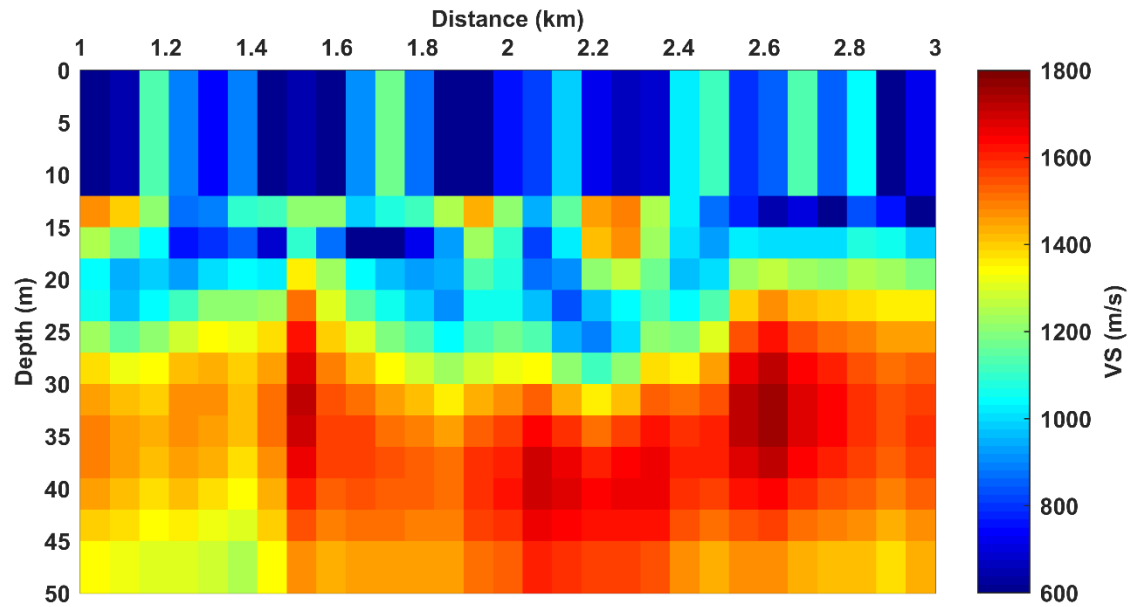


Figure 3.21: Inverted model for Inversion 4 (inversion parameters in table 3.2).

The computed global misfit corresponding to each iteration in this inversion (using equation 3.2) is shown in figure 3.22. It is equal to 88.63 m/s at the last iteration. Although the misfit has increased, but this increase is still considered within the range of the misfits of previous inversions.

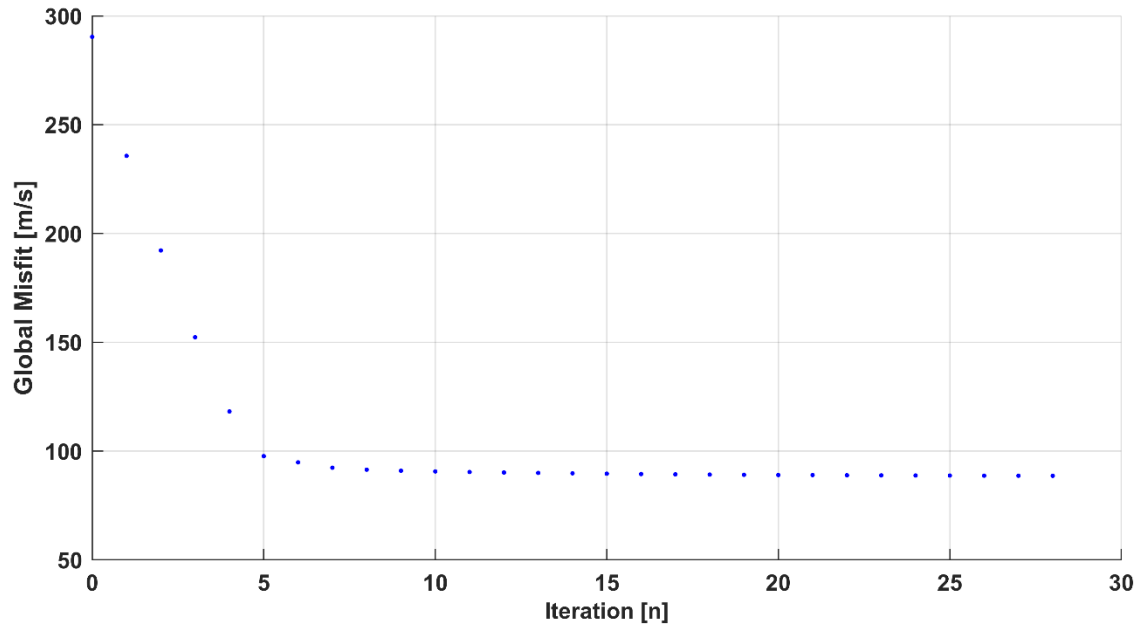


Figure 3.22: Misfit corresponding to the 4th inversion. 28 iterations needed to reach the lowest misfit.

Figure 3.23 shows the individual misfit corresponding to each path of inversion 4 calculated using equation 3.3. The highest and the lowest misfits (32.05 and 0.98) were encountered for paths 51 and 193 respectively, are highlighted by a red circle. Path numbers 209 and 220 are shown in green (1.08) and black (4.65) respectively.

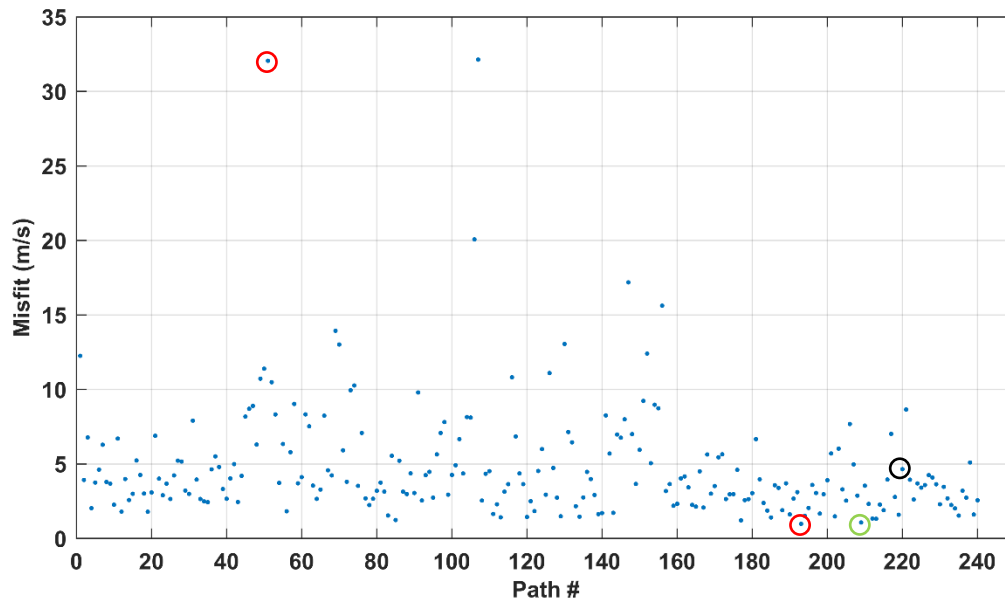


Figure 3.23: Misfit of the DCs of different paths for inversion 4.

The phase velocities in the data coverage plot shown in figure 3.10 suggest a strong lateral variation at position 2 km which connects two smoothly varying zones. The phase velocities of the DCs are slower between position 1 to 2 km compared to the rest of the investigated section (2 to 3 km). This realization is also observed in the final results of previous studies on the same dataset. Khosro Anjom et al. (2019) clustered the DCs formerly computed by Karimpour (2018) using a multi-channel processing method, and the clusters showed two different zones separated at position 2 km. In addition, the surface wave 1D inversion performed by Masoni (2016) exhibits a strong lateral variation approximately at similar position in the estimated VS model (figure 3.24). LCI is inherently suitable for situations where strong lateral variation is not expected (Socco et al., 2009). So, in inversion 2,3 and 4, where lateral constrained were used along the whole model, the strong lateral variation in the middle of the model was not properly recovered. To resolve the issue, we performed another inversion using lateral constraint equal to 100 m/s, but we broke the constraint at position 2 km. This means that we broke the link between the left side and right side of the model but kept the constraints inside each zone.

3.3.3.5 Inversion 5: broken lateral constraint equal to 100 m/s

The same homogeneous initial model is used for this inversion (figure 3.11). The estimated VS model is shown in figure 3.24a where it is compared with the VS results computed by Khosro Anjom et al., 2019 and Masoni (2016), respectively.

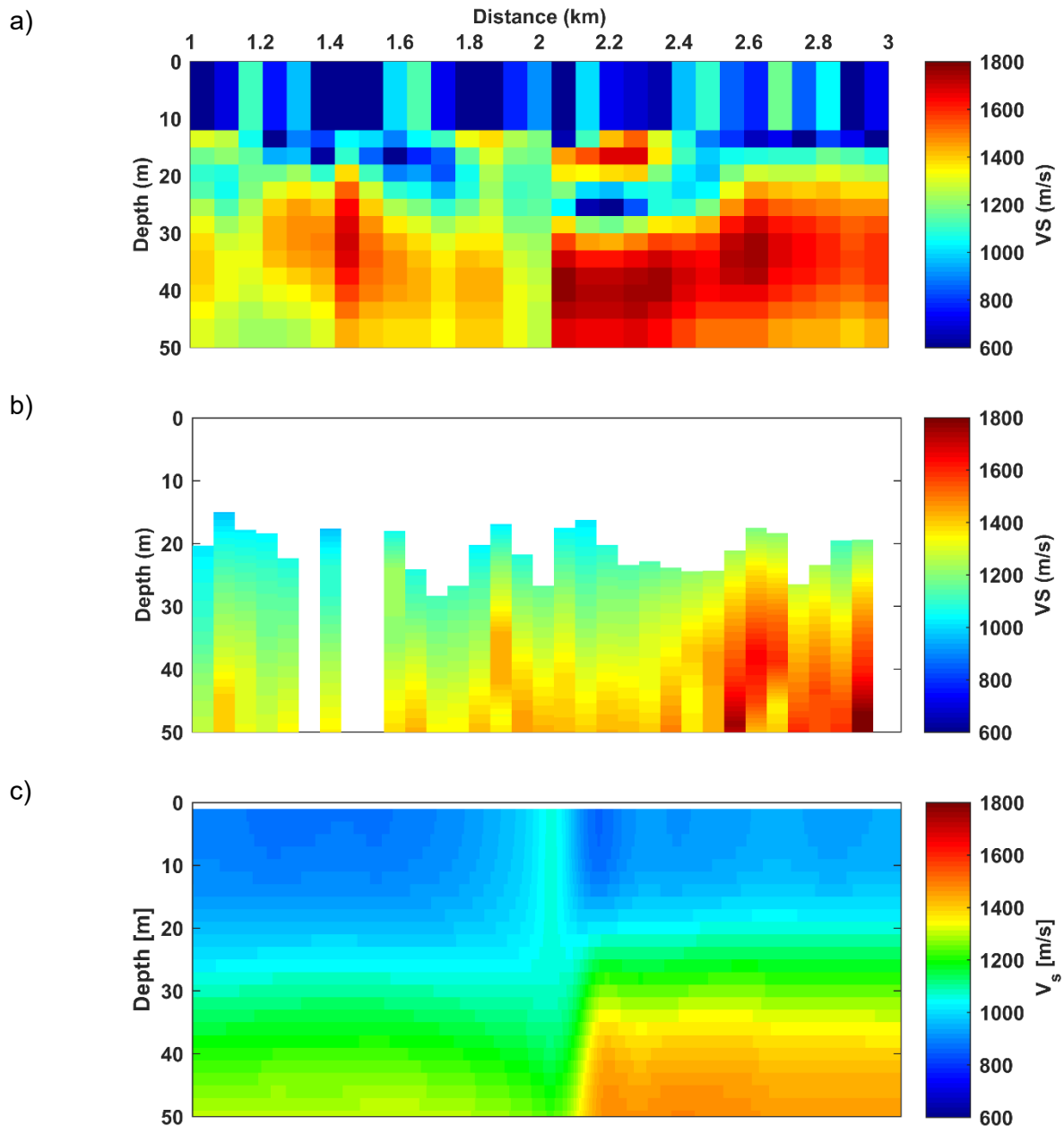


Figure 3.24: Comparison between 2D VS models obtained by a) surface wave tomography, b) surface wave direct transform (Khosro Anjom et al., 2019) and c) SWODI (Masoni, 2016).

The three methods were able to recover the strong lateral VS variations at approximately 2 km. In all three estimations, the right side of the model (2 to 3 km) shows relatively higher VS compared to the left side (1 to 2 km). The surface wave tomography shows a high-resolution in recovering the lateral variation. There is a strong resemblance between VS model from surface wave tomography (figure 3.24) and the VS from direct transform method. However, the surface wave tomography provides also estimates of the shallowest parts of the model. The SWODI estimated VS shows lower velocity estimation for the whole model, compared to the other two methods.

The global misfit corresponding to this inversion is shown in figure 3.25 is calculated according to equation 3.2 and it is equal to 87.6 m/s at the last iteration. It decreased compared to the inversion of 100 m/s without breaking the constraint and still in the range of previous inversions which means that it did not over-smooth the model.

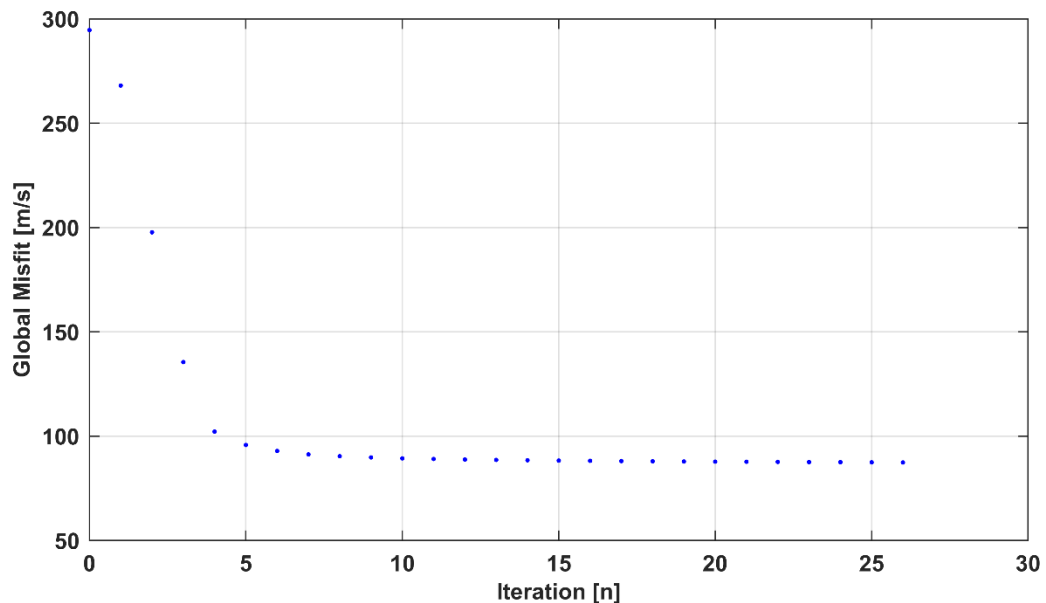


Figure 3.25: Misfit corresponding to the 5th inversion. 26 iterations needed to reach the lowest misfit.

The individual misfit corresponding to each path of inversion 5 shown in figure 3.24a, is shown in figure 3.26, the highest and lowest misfit correspond to paths number 51

(35.55) and 209 (1.05) and are highlighted in red whereas the green and the black circles show the paths number 193 (1.1) and 220 (4.23) respectively.

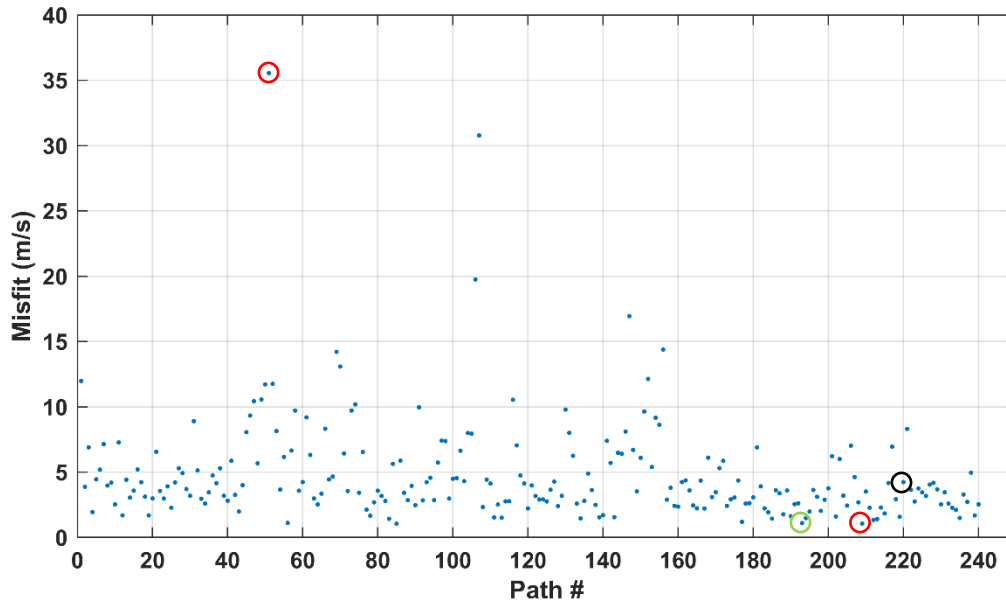


Figure 3.26: Misfit of the DCs of different paths for inversion 5.

All laterally constrained inversions exhibit slightly (less than 3 percent) higher total average misfit for the individual paths.

Figure 3.27 shows the fitting of the DCs corresponding to path number 51 according to different inversions. The misfit has increased with increasing the constraints. The DCs fitting of path 51 showed the highest registered misfits among all paths and it is expected to be an outlier DC.

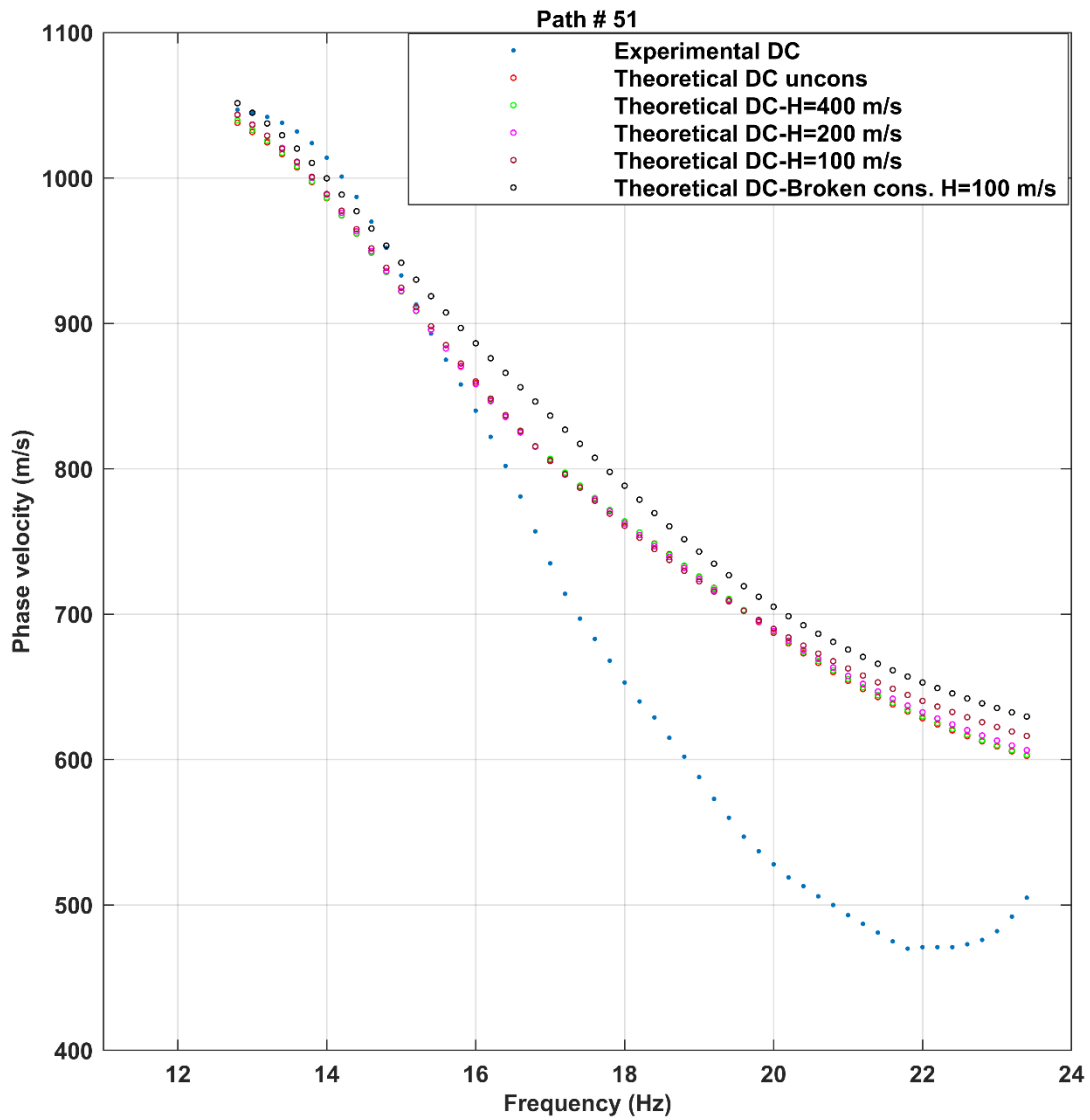


Figure 3.27: Fitting of experimental and theoretical DCs for path number 51 for different inversions.

The fitting of the DCs corresponding to the path number 193 for different inversions is shown in figure 3.28. The misfit is approximately the same for all the inversions, even after increasing the constraints.

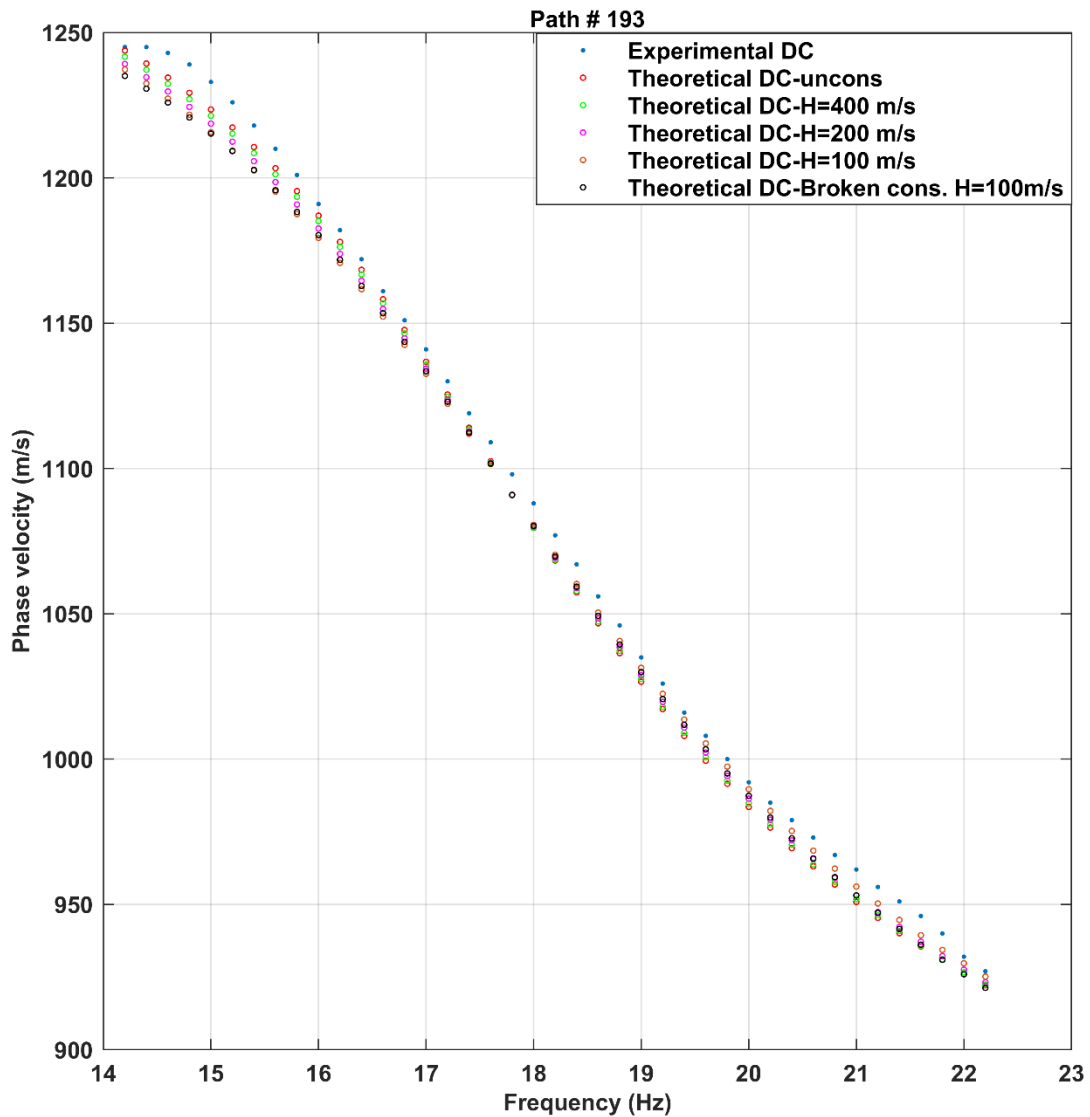


Figure 3.28: Fitting of experimental and theoretical DCs for path number 193 for different inversions.

Figure 3.29 shows the fitting of the DCs for path number 209 for all the inversions. It is noticed that the lowest misfit is registered for inversion 5 where we broke the constraint. However, all the five inversions have misfits within the same range.

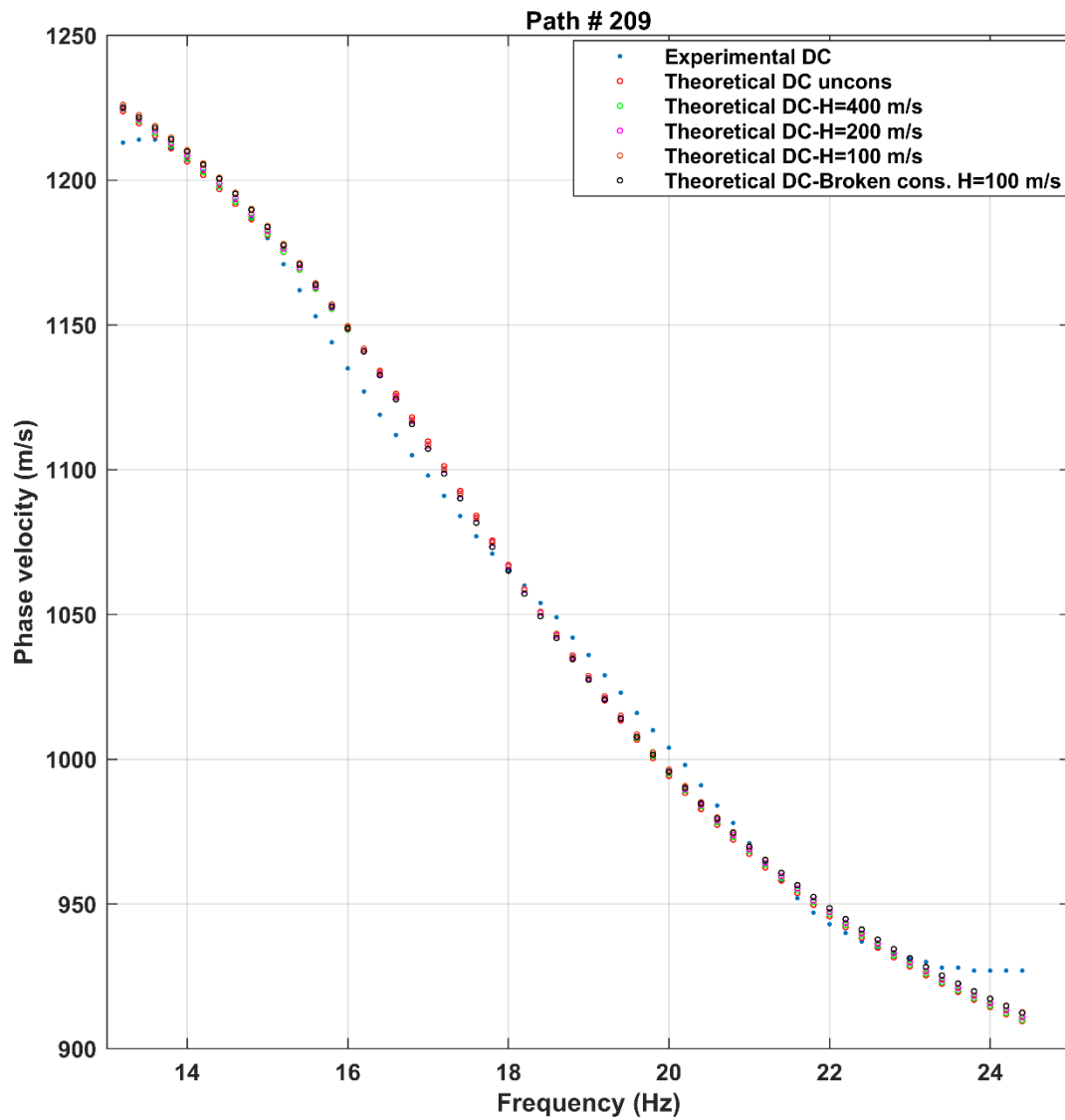


Figure 3.29: Fitting of experimental and theoretical DCs for path number 209 for different inversions.

Figure 3.30 shows the DCs fitting of the path 220. Even though the misfit is approximately the same for different inversions after increasing the lateral constraints, the lowest is registered for inversion 5.

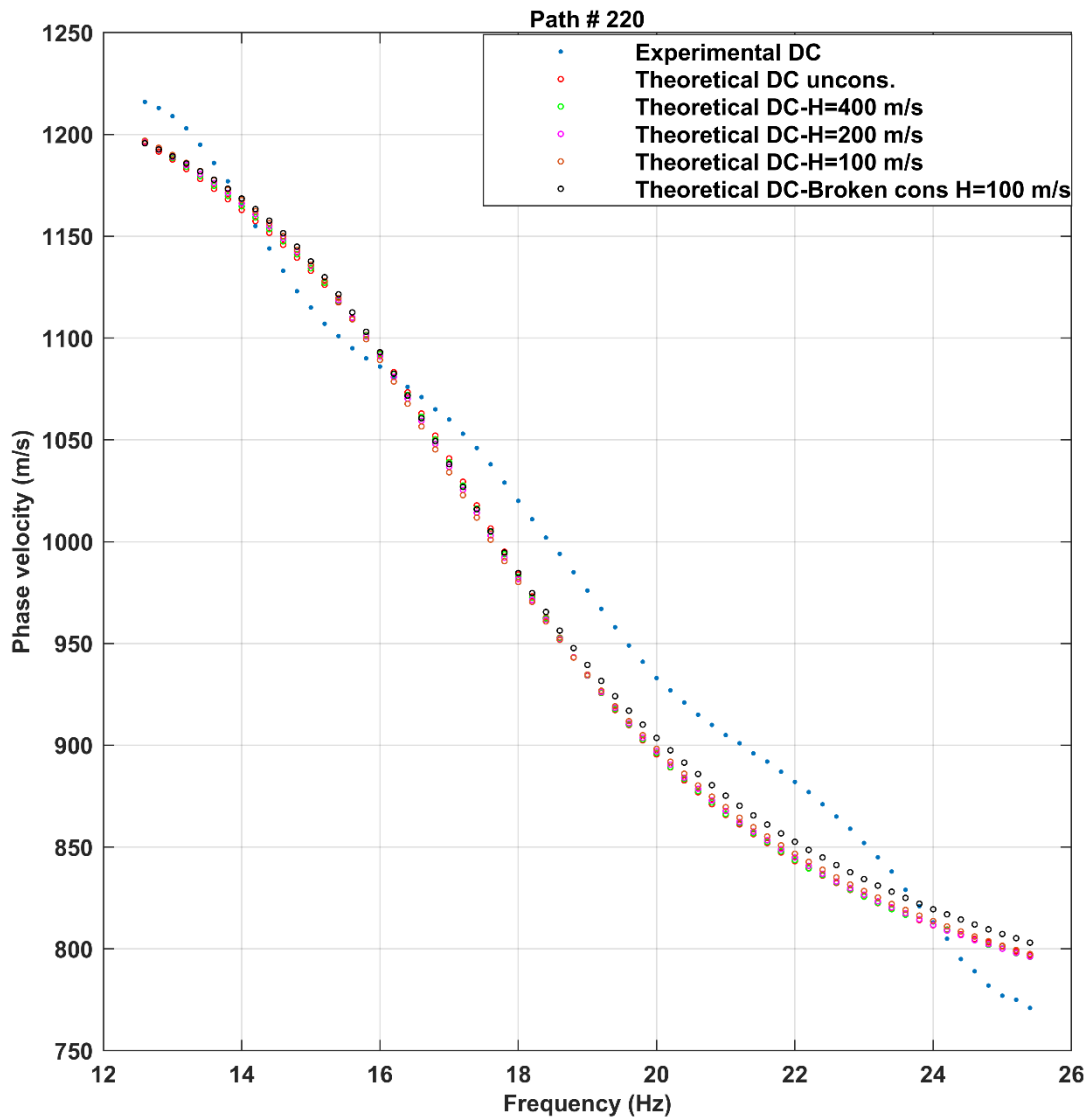


Figure 3.30: Fitting of experimental and theoretical DCs for path number 220 for different inversions.

3.3.4 Checkerboard test

The achievable resolution of the tomographic inversion, as shown in the method chapter, is evaluated by the checkerboard test. The settings of the checkerboard test are reported in table 3.3.

Checkerboard number	1
Settings	
Number of layers	12 + half space
Model points	30
Perturbation (%)	15
Perturbation spacing (model points by number of layers)	2x2

Table 3.3: The settings for the checkerboard test.

The initial VS model for the checkerboard test is shown in figure 3.31. It is generated by the forward model illustrated in the method chapter by specifying the model parameters (number of layers, density, Poisson ratio as well as its VS). Its VS is computed by taking the average velocity of each layer of the inversion of real data of inversion 5 and shown as 30 1D VS models along the receiver line.

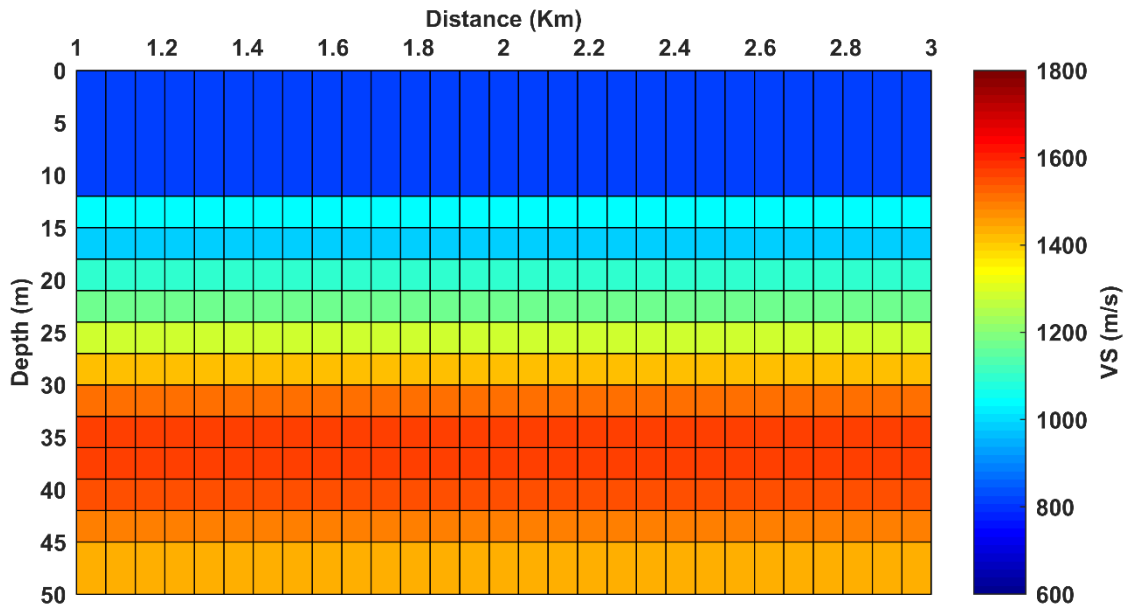


Figure 3.31: Checkerboard initial VS model.

The perturbation percentage as well as its block size applied to the initial VS model is shown in figure 3.32. It is equal to 15 percent with alternated stripe size (2 model points by 2 layers).

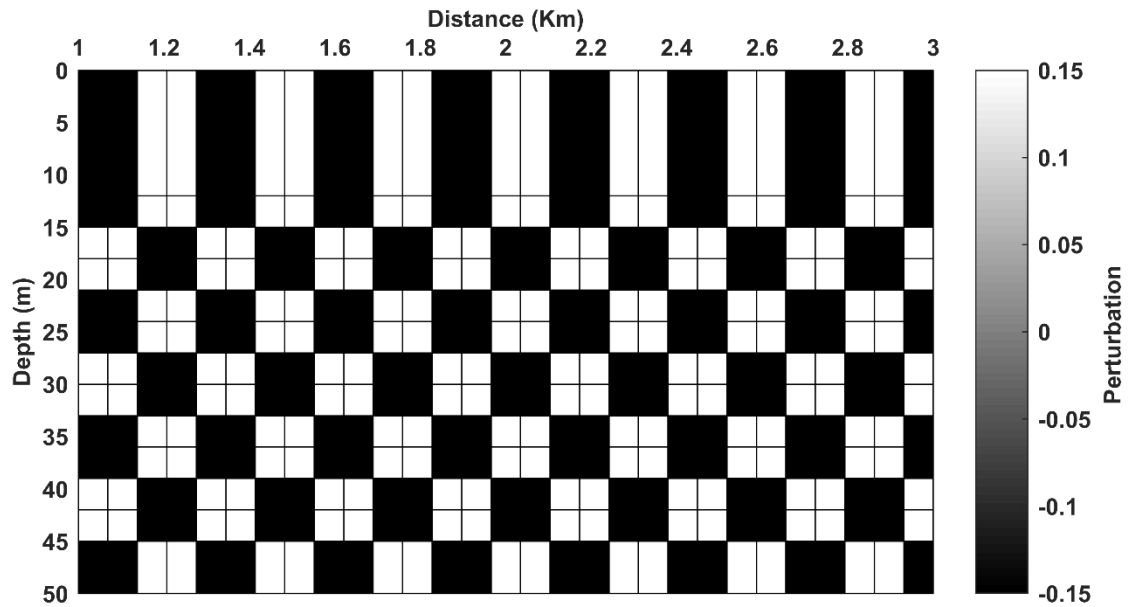


Figure 3.32: Scheme of positive and negative 15 percent perturbation.

Figure 3.33 shows the perturbed model obtained by applying the perturbation on the initial VS model shown in figure 3.31).

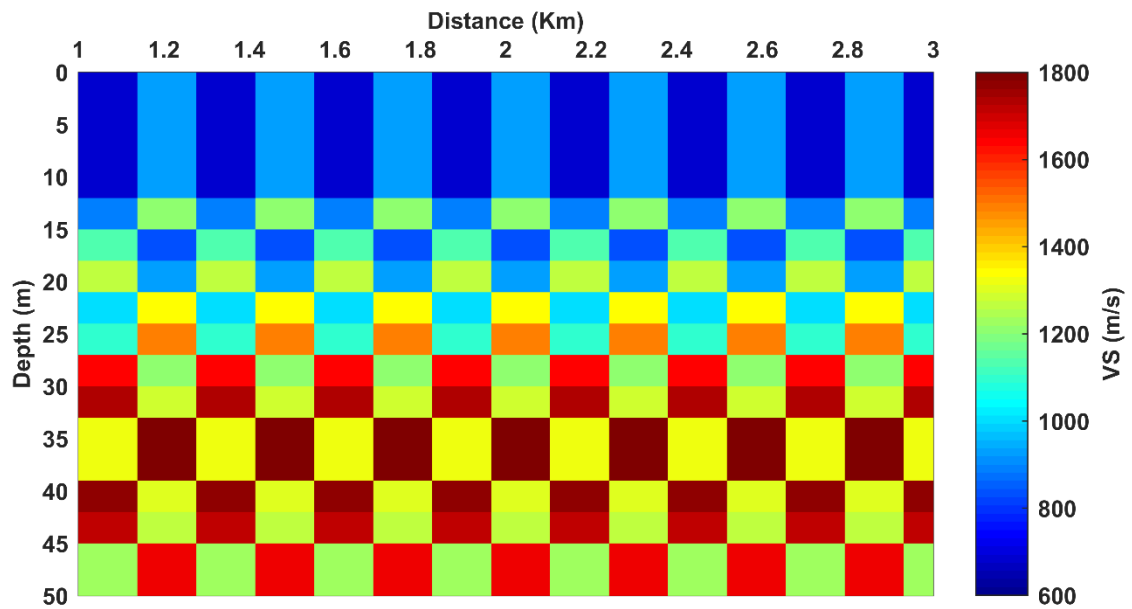


Figure 3.33: Perturbed model obtained by the multiplication of the initial model by the perturbation.

The inverted model is shown in figure 3.34. The VS estimated by the inverted model is similar to the VS in the perturbed model for all the layers. Hence, the perturbations applied to the initial model were recovered in relatively high-resolution.

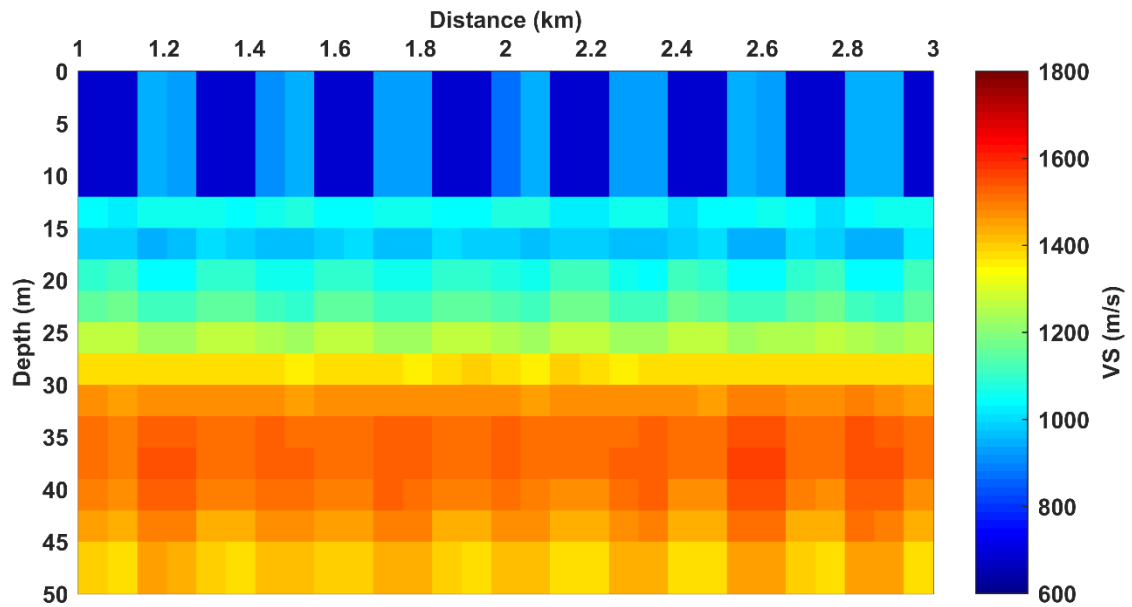


Figure 3.34: Inverted model obtained by the checkerboard test.

The global misfit calculated as in equation 3.2 is shown in figure 3.35. It drops to a value close to zero after 28 iterations.

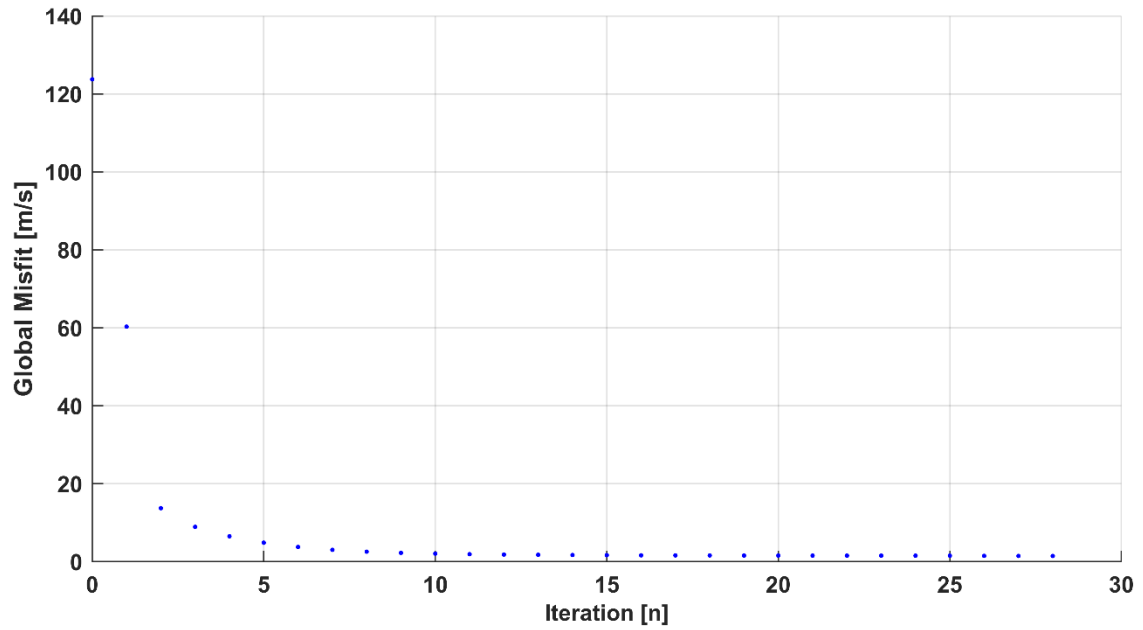


Figure 3.35: Misfit corresponding to the checkerboard test. 28 iterations needed to reach the lowest misfit.

Chapter 4: Discussion and Conclusion

Surface wave tomography is a powerful tool to estimate the VS model. We showed an application of multiple surface wave tomographic inversion to a 2D data, acquired for oil and gas exploration purposes.

The DCs were extracted by computing the average phase slowness for each receiver pair illuminated by a source. The multiple tests we performed for optimizing the processing parameters, revealed that the optimal distance between the source and the first receiver is 150m (Appendix A). The tests also showed that the optimal inter-receiver offset to provide a good quality cross-multiplication matrix while respecting the wavelength range of the surface wave, is 60 to 140 m (Appendix A). It is worth mentioning that the processing parameters are highly affected by the acquisition layout and characteristics of the site. Picking multiple DCs for each shot (60 to 140 m) inter-receiver offset and sliding the paths 40 m at a time, resulted in a good and uniform data coverage.

The DCs estimated corresponding to the multiple paths showed high phase velocity ranging from 700 to 1300 m/s, which produced relatively broad band wavelengths ranging from 20 to 120 m. Thanks to large wavelengths, we were able to estimate the VS up to 50 m in depth. A novel method related to the coverage was implemented in this study. It showed the lateral velocity changes on a phase velocity vs wavelength plot where the available paths (corresponding to each receiver pair) are plotted according to their phase velocity within the wavelength range.

We performed an unconstrained inversion and multiple laterally constrained inversions with different level of constraints. The unconstrained inversion presented high and inconsistent variations which confirmed the necessity of imposing lateral constraints. The second inversion, for a lateral constraint equal to 400 m/s, did not improve the model since 400 m/s is considered weak constraint for this geological structure. The inversions for lateral constraints of 200 and 100 m/s achieved a more consistent VS model. However, they were not able to recover the strong lateral variations (in the

middle of the line) which was illustrated by previous studies (Masoni 2016; Khosro Anjom et., al 2019) and the data coverage showing the phase velocity variation (figure 3.10). We used this information and performed the laterally constrained inversion (100 m/s) and breaking the constraints at position 2 km where the strong lateral variation was suggested. The results of inversion 5 showed smooth and consistent VS model while the strong lateral variation was perfectly evident between each side of the model (figure 3.24a). The breaking of the constraints led to slightly lower global misfit, compared to the continuous laterally constrained inversion.

Increasing the lateral constraints slightly increased the misfit of most of the paths that are shown for different inversions. However, it is considered within the same range for all the inversions. The global misfit constantly increased from inversion 1 (86.3 m/s) to inversion 4 (88.6 m/s) then it decreased to 87.6 m/s in inversion 5 after breaking the constraints.

The comparison between the final result of the surface wave tomography (inversion 5) with the VS results of the previous study by Khosro Anjom et al. (2019) and Masoni (2016) showed strong similarity. However, the VS model by Masoni (2016) showed lower overall velocity with respect to the other two estimations. All three estimated models, show a strong variation at position 2 km. The VS at the right side of the models (2 to 3 km) show relatively higher velocity compared to the left side of the models (1 to 2 km).

We performed a checkerboard test that showed a high resolution in recovering the perturbations.

REFERENCES

- [1] Al-Anezi, G. T., A. M., Al-Amri, and H., Zaman, 2011. Investigation of the weathering layer using seismic refraction and high-resolution seismic reflection methods, NE of Riyadh city. *Arabian Journal of Geosciences*, 5(6), 1347–1358. doi:10.1007/s12517-011-0290-y
- [2] Athanapoulus, G.A., P.E., Pelekis, and G.A., Anagnostopoulos, 2000. Effect of soil stiffness in the attenuation of Rayleigh wave motions from field measurements. *Soil Dynamics and Earthquake* 19, 277-288.
- [3] Auken, E., and A.V., Christiansen, 2004. Layered and laterally constrained 2D inversion of resistivity data, *Geophysics*, 69, 752—761, doi:10.1190/1.1759461.
- [4] Bao, X., X., Song, and J., Li, 2015. High-resolution lithospheric structure beneath Mainland China from ambient noise and earthquake surface-wave tomography. *Earth and Planetary Science Letters*, 417, 132-141. doi:10.1016/j.epsl.2015.02.024
- [5] Berni, A. J., and W.L., Roever, 1989. Field array performance: Theoretical study of spatially correlated variations in amplitude coupling and static shift and case study in the Paris basin: *Geophysics*, 54, 451 – 459, doi:10.1190/1.1442671.
- [6] Bloch, S., and A. L., Hales, 1968. New techniques for the determination of surface wave phase velocities: *Bulletin of the Seismological Society of America*, 58, no.3, 1021-1034.
- [7] Boiero, D., 2009. *Surface Wave Analysis for Building Shear Wave Velocity Models*: Ph.D. Thesis, Politecnico di Torino.
- [8] Boiero, D., and L.V., Socco, 2010. Retrieving lateral variations from surface wave dispersion curves, *Geophysical Prospecting*, doi: 10.1111/j.1365-2478.2010.00877.x
- [9] Braile L.W., 2006. *Seismic Waves and the Slinky: A Guide for Teachers*. Department of Earth, Atmospheric, and Planetary Sciences Purdue University. West Lafayette, IN , Available in: <<https://web.ics.purdue.edu/~braile/edumod/slinky/slinky.htm>>.
- [10] Burger HR, A.F., Sheehan, and C.H., Hones, 1992. *Introduction to Applied Geophysics: Exploration of the Shallow Subsurface*, 65p
- [11] Dobrin, M. 1950. Dispersion in seismic surface waves. In 20th Annual SEG Meeting (Chicago).
- [12] Dziewonski, A., S. Bloch and M. Landisman, 1969. A technique for the analysis of transient seismic signals: *Bulletin of the Seismological Society of America*, 59 n.1, 427-444.

- [13] Da Col, F., 2013. Surface Wave Tomography at Exploration Scale. MSc Thesis.
- [14] Evans, B. J., and W.H. Dragoset, 1997. A handbook for seismic data acquisition in exploration. Tulsa, OK: Society of Exploration Geophysicists.
- [15] Feng, M. and M., An, 2010. Lithospheric structure of the Chinese mainland determined from joint inversion of regional and teleseismic Rayleigh-wave group velocities. *J. Geophys. Res.*115. doi:10.1029/2008JB005787.
- [16] Foti, S., F., Hollender, F., Garofalo, Bull Earthquake Eng (2018) 16: 2367. doi:10.1007/s10518-017-0206-7.
- [17] Fu, Y. V., L., Li, and Z. Xiao, 2019. Lithospheric SH wave velocity structure beneath the northeastern Tibetan plateau from Love wave tomography. *Journal of Geophysical Research: Solid Earth*, 124. doi:10.1029/ 2019JB017788
- [18] Haskell, N. 1953. The dispersion of surface waves on multilayered media. *Bulletin of the Seismological Society of America*, 43(0037-1106), 17-34. Retrieved from <http://bssa.geoscienceworld.org/content/43/1/17>
- [19] Iglesias, A., R. W. Clayton, X. Pérez-Campos, S. K. Singh, J. F. Pacheco, D. García, and C. Valdés-González 2010. S-wave velocity structure below central Mexico using high-resolution surface wave tomography, *J. Geophys. Res.*,115, B06307, doi:10.1029/2009JB006332.
- [20] Ikeda, T. and T., Tsuji, Surface-wave tomography for near-surface characterization with continuous wavelet transform for two-station cross-correlation, in SEG Technical Program Expanded Abstract 2018, accepted. doi:10.1190/segam2018-2996939.1.
- [21] Jones, R. B., 1958. In-situ measurement of the dynamic properties of soil by vibration methods: *Geotechnique*, 8, 1–21, doi:10.1680/geot.1958.8.1.1
- [22] Karimpour, M. 2018. Processing Workflow for Estimation of Dispersion Curves from Seismic Data and QC. MSc thesis, Politecnico di Torino
- [23] Kästle, Emanuel D., A. El-Sharkawy, L., Boschi, T., Meier, C., Rosenberg, N., Bellahsen, and C., Weidle, 2018. Surface Wave Tomography of the Alps Using Ambient-Noise and Earthquake Phase Velocity Measurements, doi:10.1002/2017jb014698.
- [24] Khosro Anjom, F., I., Masoni, and L.V., Socco, 2019. Application of Surface Wave Direct Transform to An Oil and Gas Exploration Data, EAGE: doi:10.3997/2214-4609.201900978.
- [25] Kugler, S., T., Bohlen, T., Forbriger, S. Bussat, and G., Gerald Klein, 2007. Scholte-wave tomography for shallow-water marine sediments, *Geophys. J. Int.*, 168, 551—570, doi:10.1111/j.1365-246X.2006.03233.x

- [26] Li, H., W., Su, C.Y., Wang, and Z., Huang, 2009. Ambient noise Rayleigh wave tomography in western Sichuan and eastern Tibet, doi:10.1016/j.epsl.2009.03.021
- [27] Maraschini, M., 2008. A new approach for the inversion of Rayleigh and Scholte waves in site characterization: Ph.D. dissertation, Politecnico di Torino.
- [28] Marquart, D., 1963. An algorithm for least squares estimation of nonlinear parameters, *Journal of the Society of Industrial Applied Mathematics*, 2, 431—441, doi:10.1137/0111030.
- [29] Masoni, I., 2016. Inversion of surface waves in an oil and gas exploration context: PhD dissertation, Universite Grenoble Alpes.
- [30] Moschetti, M. P., M. H. Ritzwoller, and N. M. Shapiro 2007. Surface wave tomography of the western United States from ambient seismic noise: Rayleigh wave group velocity maps, *Geochem. Geophys. Geosyst.*,8, Q08010, doi:10.1029/2007GC001655.
- [31] Papadopoulou M., F., Da Col, B., Mi, E., Backstrom, P., Marsden, B., Brodic, A., Malehmir, and L.V., Socco, 2019. Surface-wave analysis for static corrections in mineral exploration: a case study from central Sweden. *Geophysical prospecting*, doi: 10.1111/1365-2478.12895
- [32] Picozzi, M., and D. Albarello, 2007. Combining genetic and linearized algorithms for a two-step joint inversion of Rayleigh wave dispersion and H/V spectral ratio curves: *Geophysical Journal International*, 169, 189–200, doi:10.1111/j.1365-246X.2006.03282.x
- [33] Salaün, G., H., Pedersen, A., Paul, V., Farra, Karabulut, D. Hatzfeld, C., Papazachos, D.M. Childs, C., Pequegnat, and the SIMBAAD Team, 2012. High resolution surface wave tomography beneath the Aegean-Anatolia region: constraints on upper mantle structure: *Geophysical J. Int.*, v. 190, p. 406-420, doi: 410.1111/j.1365- 1246X.2012.05483.x
- [34] Shapiro, N.M., M.H. Ritzwoller, P. Molnar, and V. Levin, 2004. Thinning and flow of Tibetan crust constrained by seismic anisotropy, *Science*, 305, 233-236, doi:10.1126/science.1098276
- [35] Shapiro, N. M., M, Campillo, L., Stehly, and M.H., Ritzwoller, 2005. High-resolution surface-wave tomography from ambient seismic noise. *Science* 307, 1615–1618, doi:10.1126/science.1108339.
- [36] Socco, L.V., and C. Strobbia, 2004. Surface-wave method for near surface characterization: a tutorial: *Near Surface Geophysics*, 2, no.4, 165-185, doi:10.3997/1873-0604.2004015.
- [37] Socco, L.V., D. Boiero, S. Foti and R. Wisen, 2009. Laterally constrained inversion of ground roll from seismic reflection records: *Geophysics*, 74 no.6, 35-45, doi:10.1190/1.3223636

- [38] Socco, L.V., S. Foti and D. Boiero, 2010. Surface-wave analysis for building near-surface velocity models -Established approaches and new perspectives: *Geophysics*, 75 no. 5, 83-102, doi:10.1190/1.3479491.
- [39] Steeples D.W., 2000. A review of shallow seismic methods. *Annali di Geofisica* 43: 1021-1044
- [40] Tarantola, A., 2005. Inverse problem theory and methods for model parameter estimation: SIAM.
- [41] Thomson, W. T., 1950. Transmission of Elastic Waves through a Stratified Solid Medium. *Journal of Applied Physics*, 21(2), 89-93. doi:10.1063/1.1699629
- [42] Villasenor, A., Y. Yang, M. H. Ritzwoller, and J. Gallart 2007. Ambient noise surface wave tomography of the Iberian Peninsula: Implications for shallow seismic structure, *Geophys. Res. Lett.*, 34, L11304, doi:10.1029/2007GL030164.
- [43] Woodhouse, J.H., and A.M., Dziewonski, 1984. Mapping the upper mantle: Three-dimensional modeling of earth structure by inversion of seismic waveforms, *J. Geophys. Res.*, 89, 5953--5986.
- [44] Yao, H., G., Xu, L., Zhu, and X., Xiao, 2005. Mantle structure from inter-station Rayleigh wave dispersion and its tectonic implication in western China and neighboring regions, *Phys. Earth planet. Inter.*, 148, 39—54, doi:10.1016/j.pepi.2004.08.006.
- [45] Yao, H., R.D. Van der Hilst, and M.V. de Hoop, 2006. Surface-wave array tomography in SE Tibet from ambient seismic noise and two-station analysis-I. Phase velocity maps, *Geophys. J. Int.*, 166, 732—744, doi:10.1111/j.1365-246X.2006.03028.x.
- [46] Yao, H., C. Beghein, and R.D., Van der Hilst, 2008. Surface-wave array tomography in SE Tibet from ambient seismic noise and two-station analysis-II. Crustal and upper mantle structure, *Geophys. J. Int.*, 173, 205—219, doi:10.1111/j.1365-246X.2007.03696.x.
- [47] Yao, H., R.D., van der Hilst, J.-P., Montagner, 2010. Heterogeneity and anisotropy of the lithosphere of SE Tibet from surface wave array tomography. *J. Geophys. Res.* 115, B12307, doi:10.1029/2009JB007142
- [48] Yao, H., 2012. Lithospheric structure and deformation in SE Tibet revealed by ambient noise and earthquake surface wave tomography: Recent advances and perspectives. *Earthq (2012) Sci* 25: 371, doi:10.1007/s11589-012-0863-1
- [49] Zheng, S., X. Sun, X. Song, Y. Yang, and M. H. Ritzwoller, 2008. Surface wave tomography of China from ambient seismic noise correlation, *Geochem. Geophys. Geosyst.*, 9, Q05020, doi:10.1029/2008GC001981.

APPENDIX A

Here we show some selected examples of processing tests used to define the optimal processing parameters. The purpose of the following examples is to prove the choice made for the offsets as well as the distance between the coupled receivers used to extract the DCs.

Since the sources and receivers are evenly spaced, the closest shot is approximately 10 m away to any receiver. Many tests were carried to choose an optimal offset from the first receiver starting from 10 m and increasing the offset 20 m continuously. For short offsets (10 m and 30 m), the frequency band of the DCs is narrow due the short distance between the shot and the receivers. For offsets higher than 310 m, the frequency band of the DCs is short as shown in the following examples. Examples 1,2 and 3 show the short, long and optimal offset range, respectively, using 5 different shots (offsets) with the same inter-receiver distance to check the effect of the offset on the DCs in order to choose an optimal offset. Examples 4 and 5 show minimum and maximum distances between receivers: we fix the shot and we perform several examples changing the inter-receiver distance to check its effect on DCs in order to choose an optimal range. The table A.1 shows the configuration for each example.

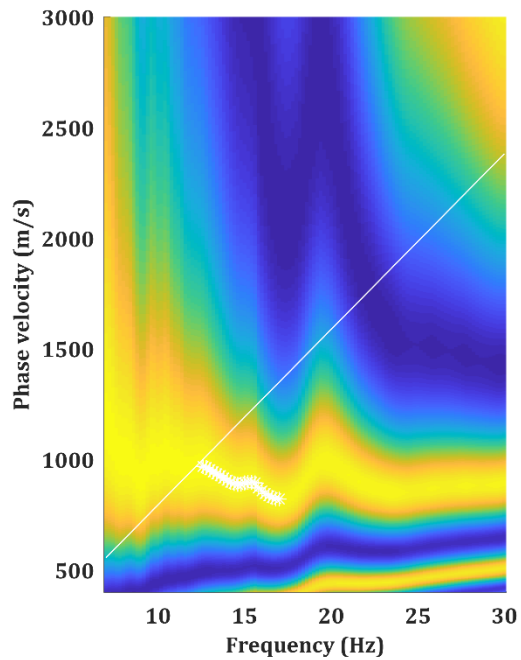
Example number	Shot number	Receiver couples	Offset (m)	Inter-receiver distance (m)
1	68	20&22	10	40
2	43	20&22	510	40
3	66	20&22	50	40
	61	20&22	150	40
	53	20&22	310	40
4	42	1&2	150	20
	42	1&3	150	40
	42	1&4	150	60
5	42	1&8	150	140
	42	1&9	150	160

Table A.1: Source and receivers' configuration for each example.

Example 1: Short offset

The figure A.1 shows a DC corresponding to a shot number 68 with receiver couple 20&22. The offset is 10 m from the first receiver. The DC shows a narrow frequency band. Thus, it only represents a small portion of the subsurface. The short offsets must be avoided for extracting DCs since they affect the frequency band.

a)



b)

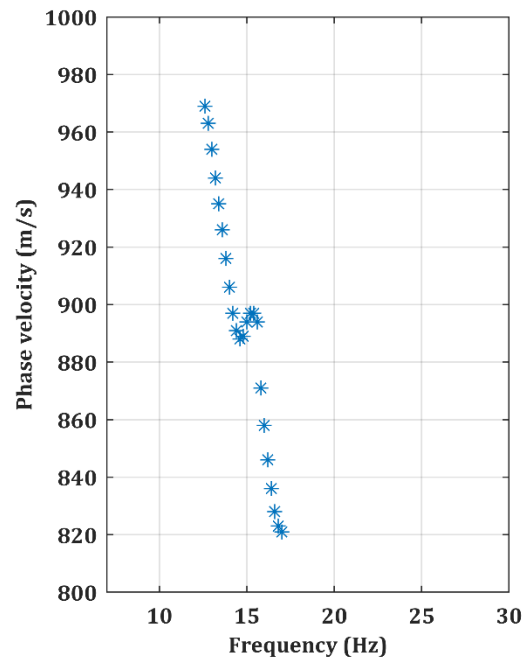
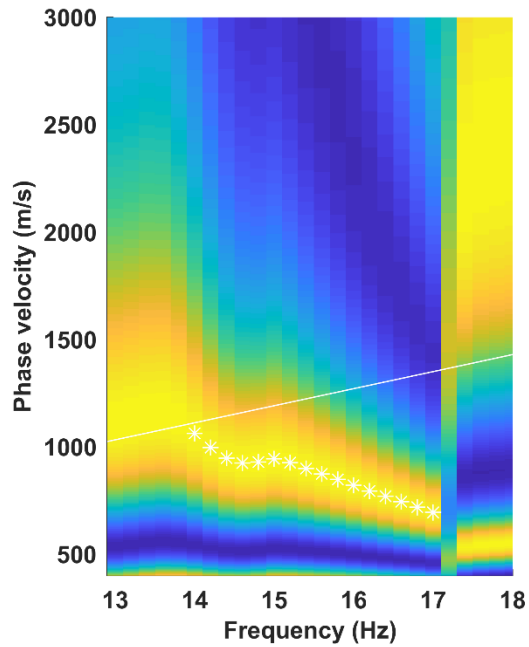


Figure A.1: DC for shot number 68 and receiver pair 20&22: a) The windowed cross multiplication matrix of the two traces b) Picked DC.

Example 2: Long offset

The figure A.2 shows a picked DC for a shot number 43 with receiver couple 20&22. The offset is 510 m from the first receiver. The curve encounters an anomaly close to 15 Hz. The frequency bandwidth range is relatively short; thus, it only represent a small portion of the subsurface. There is a restriction on the maximum offset to be used.

a)



b)

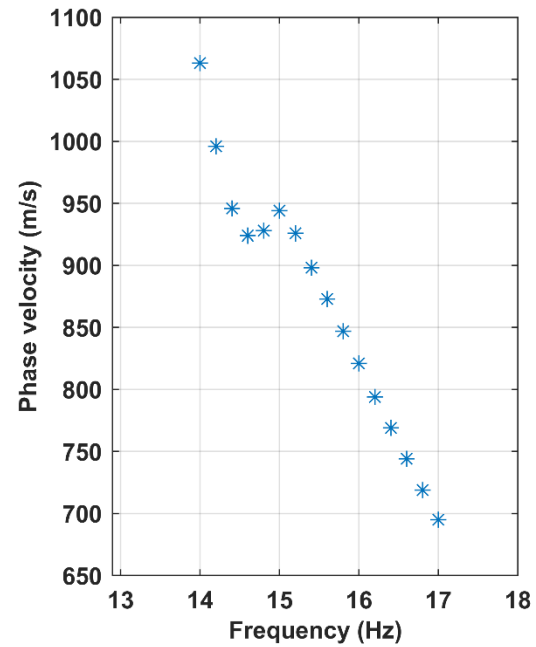
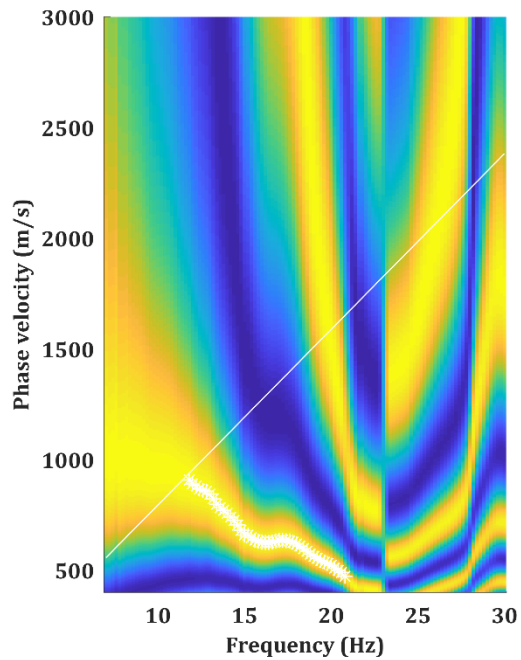


Figure A.2: DC for shot number 43 and receiver pair 20&22: a) The windowed cross multiplication matrix of the two traces b) Picked DC.

Example 3: Optimal offset range

An example is given in figure A.3 showing a DC corresponding to a shot number 66 with receiver couple 20&22. The offset is 50 m from the first receiver. The frequency band is relatively large compared to previous examples. This is the minimum offset of the optimal offset range.

a)



b)

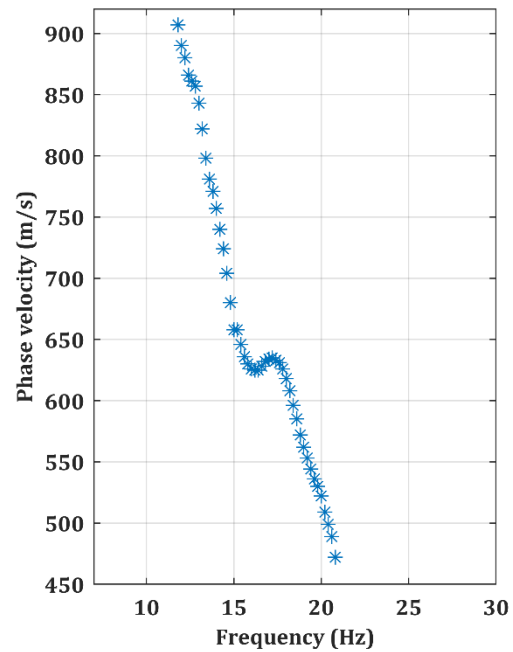


Figure A.3: DC for shot number 66 and receiver pair 20&22: a) The windowed cross multiplication matrix of the two traces b) Picked DC.

The figure A.4. shows a picked DC for a shot number 61 and receiver couple 20&22. The offset is 150 m from the first receiver. The curve has a wide frequency range between 13 Hz and 21 Hz compared to other offsets and it does not encounter any discontinuity or anomaly within this range.

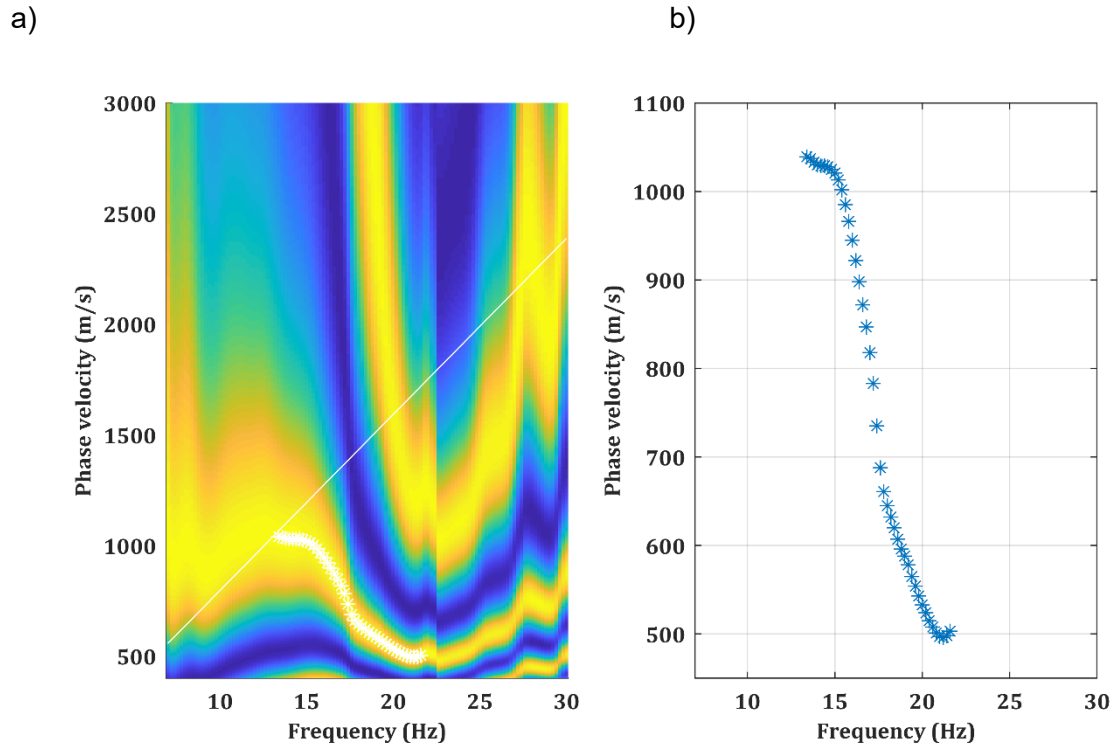


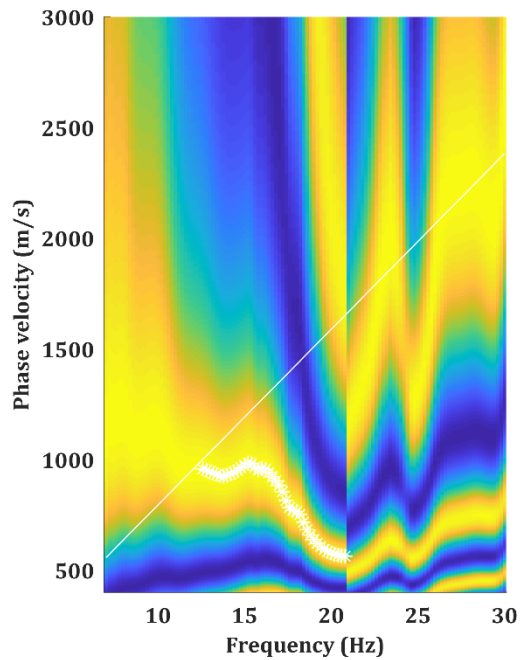
Figure A.4: DC for shot number 61 and receiver pair 20&22: a) The windowed cross multiplication matrix of the two traces b) Picked DC.

The figure A.5. shows a picked DC for a shot number 53 and receiver couple 20&22. The offset is 310 m from the first receiver. The frequency band is relatively wide.

Above this offset, the frequency band starts to decrease, and no further information can be added.

The optimal offset range is between 50 m and 310 m. The offset chosen for the extraction of the DCs is 150 m since it has the best quality within the optimal offset range.

a)



b)

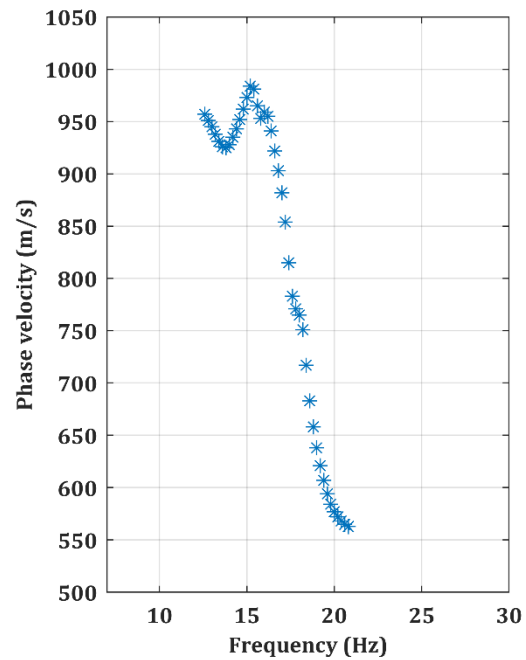
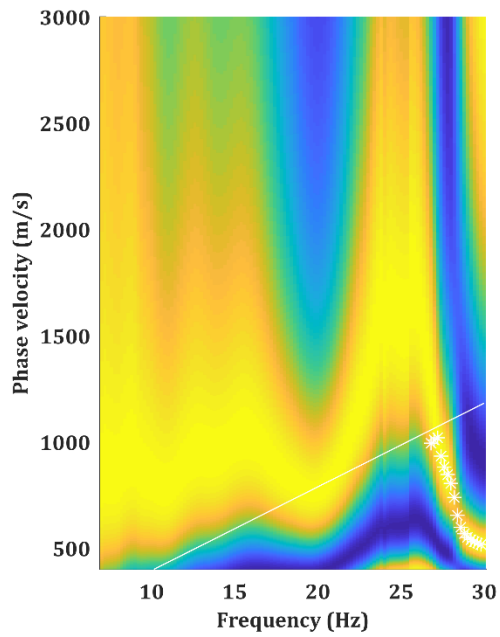


Figure A.5: DC for shot number 53 and receiver pair 20&22: a) The windowed cross multiplication matrix of the two traces b) Picked DC.

Example 4: Minimum inter-receivers distance

The quality of the DC depends also on the receiver spacing. As shown in figure A.6, the receiver spacing is equal to 20 m. Above the white line plotted on the spectrum, the phase velocity picking is not reliable. This line depends on the receiver spacing. The frequency band is very narrow.

a)



b)

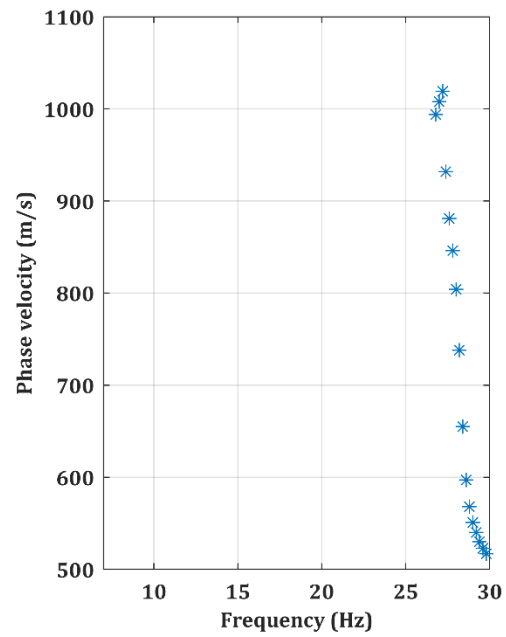
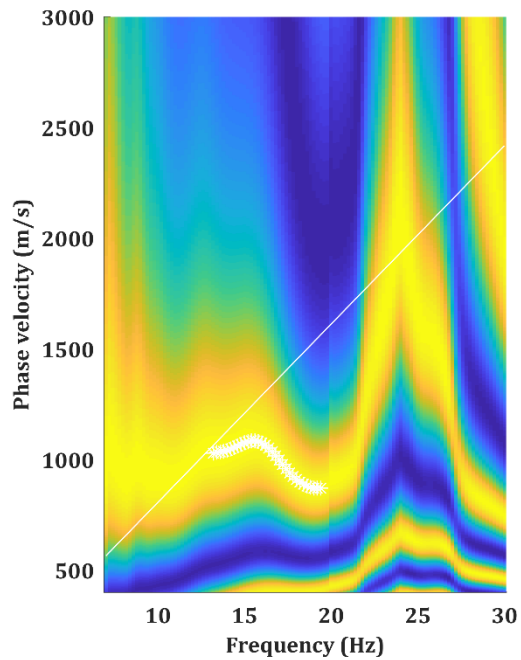


Figure A.6: DC for shot number 42 and receiver pair 1&2: a) The windowed cross multiplication matrix of the two traces b) Picked DC.

The figure A.7 shows a receiver spacing equal to 40 m. The frequency bandwidth is larger than in the figure A.6 but is still considered relatively narrow. This means that only a small portion of the subsurface will be analyzed.

a)



b)

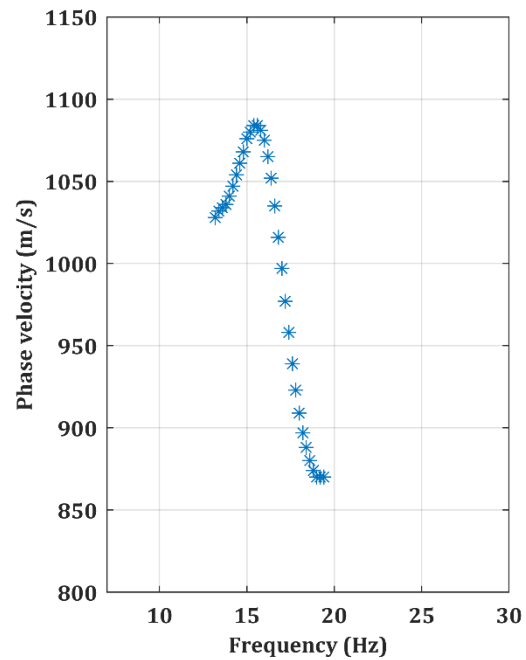
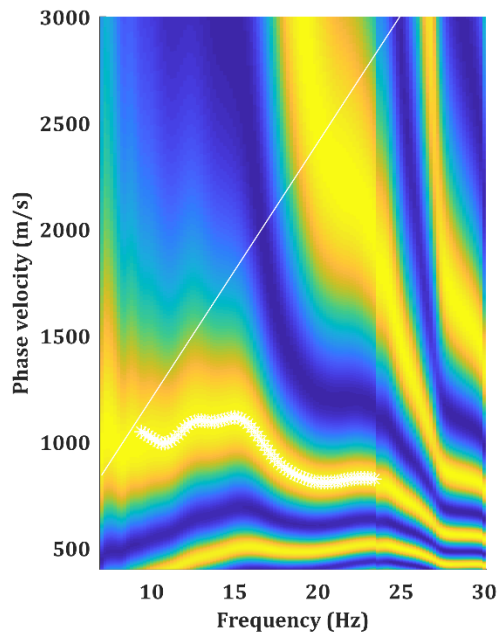


Figure A.7: DC for shot number 42 and receiver pair 1&3: a) The windowed cross multiplication matrix of the two traces b) Picked DC.

The figure A.8 shows a receiver spacing equal to 60 m. Although it has an anomaly below 15 Hz, it shows a good quality of DCs compared to lower distance between receivers in previous examples as well as the frequency band of the DC is wider.

a)



b)

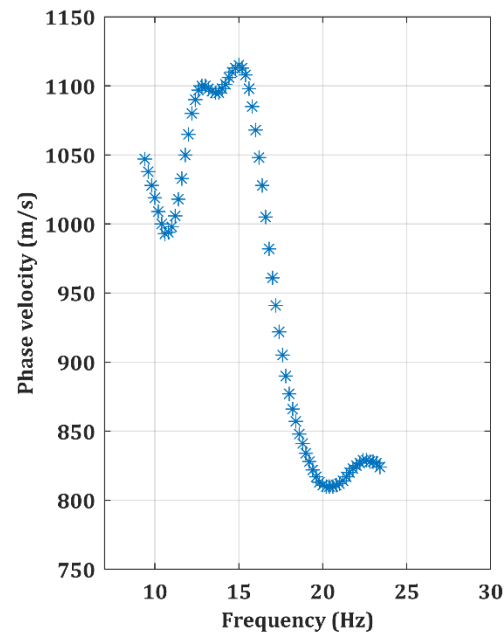


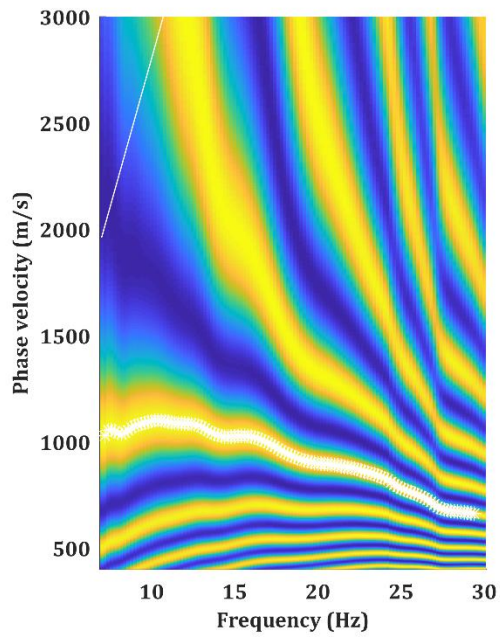
Figure A.8: DC for shot number 42 and receiver pair 1&4: a) The windowed cross multiplication matrix of the two traces b) Picked DC.

The 20 m and 40 m receiver spacing is too short to be used to extract the DCs for two-station method for this specific dataset. The minimum inter-receivers distance to be used is 60 m that present a wide frequency band compared to shorter spacing.

Example 5: Maximum inter-receivers distance

The figure A.9 shows an inter-receivers spacing equal to 140 m, where the DC has a wide frequency range. It encounters anomaly below 10 Hz but quite smooth above 10 Hz.

a)



b)

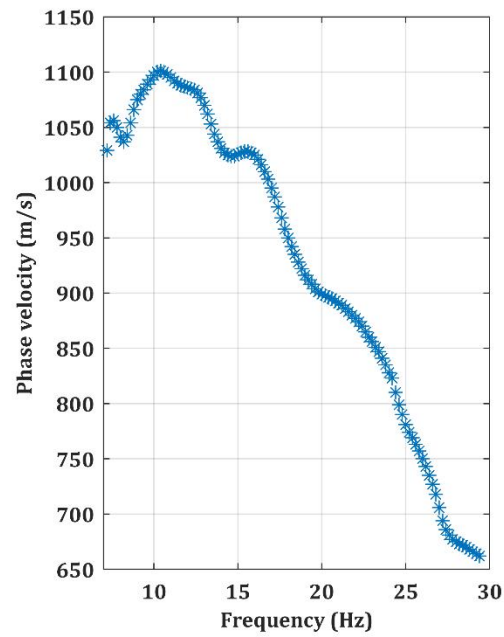
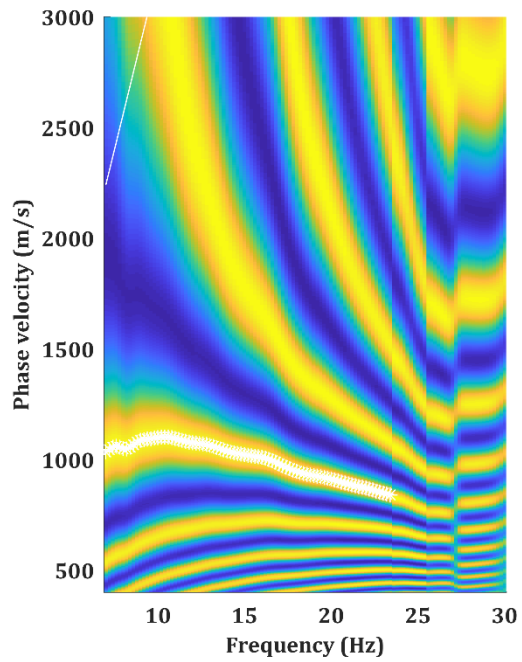


Figure A.9: DC for shot number 42 and receiver pair 1&8: a) The windowed cross multiplication matrix of the two traces b) Picked DC.

The figure A.10 shows an inter-receiver spacing equal to 160 m, where the frequency bandwidth is reduced compared to the spacing equal to 140m. There is no need to go further than 140 m since no new information can be added.

The maximum receiver spacing selected for the processing of the whole dataset is 140 m.

a)



b)

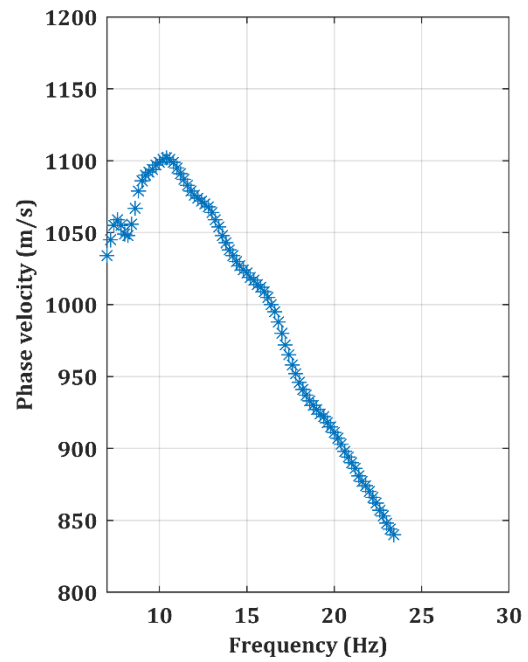


Figure A.10: DC for shot number 42 and receiver pair 1&9: a) The windowed cross multiplication matrix of the two traces b) Picked DC.